Monthly Notices
of the
ROYAL ASTRONOMICAL SOCIETY

MNRAS **492,** 3440–3458 (2020)
Advance Access publication 2020 January 11

doi:10.1093/mnras/staa074

Detectability of embedded protoplanets from hydrodynamical simulations

E. Sanchis [1,2★] G. Picogna [2] B. Ercolano,[2,3] L. Testi[1,3,4] and G. Rosotti [5,6]

[1]*European Southern Observatory, Karl-Schwarzschild-Strasse 2, D-85748 Garching bei München, Germany*
[2]*Universitäts-Sternwarte, Ludwig-Maximilians-Universität München, Scheinerstrasse 1, D-81679 München, Germany*
[3]*Excellence Cluster Origins, Boltzmannstrasse 2, D-85748 Garching bei München, Germany*
[4]*INAF/Osservatorio Astrofisico di Arcetri, Largo E. Fermi 5, I-50125 Firenze, Italy*
[5]*Institute of Astronomy, University of Cambridge, Madingley Road, Cambridge CB3 0HA, UK*
[6]*Leiden Observatory, Leiden University, PO Box 9531, NL-2300 RA Leiden, the Netherlands*

Accepted 2020 January 8. Received 2020 January 8; in original form 2019 August 9

ABSTRACT

We predict magnitudes for young planets embedded in transition discs, still affected by extinction due to material in the disc. We focus on Jupiter-sized planets at a late stage of their formation, when the planet has carved a deep gap in the gas and dust distributions and the disc starts to being transparent to the planet flux in the infrared (IR). Column densities are estimated by means of three-dimensional hydrodynamical models, performed for several planet masses. Expected magnitudes are obtained by using typical extinction properties of the disc material and evolutionary models of giant planets. For the simulated cases located at 5.2 au in a disc with a local unperturbed surface density of 127 g cm^{-2}, a 1$M_{\rm J}$ planet is highly extinct in the *J*, *H,* and *K* bands, with predicted absolute magnitudes $\geq$ 50 mag. In the *L* and *M* bands, extinction decreases, with planet magnitudes between 25 and 35 mag. In the *N* band, due to the silicate feature on the dust opacities, the expected magnitude increases to $\sim$40 mag. For a 2$M_{\rm J}$ planet, the magnitudes in the *J*, *H,* and *K* bands are above 22 mag, while for the *L*, *M,* and *N* bands, the planet magnitudes are between 15 and 20 mag. For the 5$M_{\rm J}$ planet, extinction does not play a role in any IR band, due to its ability to open deep gaps. Contrast curves are derived for the transition discs in CQ Tau, PDS 70, HL Tau, TW Hya, and HD 163296. Planet mass upper limits are estimated for the known gaps in the last two systems.

Key words: hydrodynamics – planets and satellites: detection – planet–disc interactions – protoplanetary discs – infrared: planetary systems.

1 INTRODUCTION

Over the past two decades, a large number of exoplanet detections have remarkably expanded and shaped the prevailing planet formation theories. Most of these discoveries have been accomplished using indirect techniques, although in a few cases detections were achieved using direct imaging (Quanz et al. 2015; Keppler et al. 2018; Reggiani et al. 2018). Direct observations are possible only for systems close enough to us, with planets far from their host stars (Rameau et al. 2015). When searching for young planets of only a few Myr, an additional problem arises: While a young planet might itself be bright enough to be detected, it will still be embedded in the primordial disc, and, thus, hidden behind large columns of dust and gas.

Studying the interaction between the disc material and the young planet during its formation is crucial to understand the ongoing processes of planet formation and its further evolution. After the initial stages of planet formation, the protoplanet is likely accreting material and still surrounded by gas and dust. Several processes – mainly internal and/or external photoevaporation, accretion on to the central star and planet, and magnetohydrodynamical winds (see the review by Ercolano & Pascucci 2017) – continuously reduce the disc material until its complete dispersal. The typical lifetimes for discs can vary considerably and are uncertain; in general, the inner disc (within a fraction of au from the central star) is expected to disperse within a few Myr (Hernández et al. 2008), even though there is potential evidence for the replenishment of the inner disc over longer time-scales (e.g. Beccari et al. 2010; Scicluna et al. 2014). The dissipation time-scales of the outer disc, which is more relevant for the direct detectability of young protoplanets, are much more uncertain. Initial Atacama Large Millimeter/submillimeter Array (ALMA) surveys suggest that the depletion of the outer disc may also proceed on a similar time-scale, following a simple estimate of disc masses based on the (sub)millimetre continuum emission from large dust grains (Ansdell et al. 2017). More detailed studies seem to imply that gas and dust depletion may be substantial even at young ages (Miotello et al. 2017; Manara, Morbidelli &

★ E-mail: esanchis@eso.org

Guillot 2018). As the disc keeps losing material, the extinction is reduced proportionally. If dust extinction has decreased enough, a detection of an embedded planet may be possible with state-of-the-art facilities observing at IR wavelengths, where the planet spectrum peaks.

Consequently, detections of protoplanets embedded in discs depend on the properties of the planet, its immediate surroundings, and also on the upper atmospheric layers of the disc. The search for indirect detections in (sub)-millimetre observations has been pursued over the past years (e.g. Piétu et al. 2006; Brown et al. 2008), more intensively once ALMA started operating (ALMA Partnership et al. 2015). Substructure like cavities, gaps, and spirals could be first observed at these wavelengths, suggesting planet–disc interaction as a plausible cause of such features (e.g. Paardekooper & Mellema 2006; Rice et al. 2006). The DSHARP large programme (Andrews et al. 2018) has confirmed that substructure is ubiquitous in large discs when observed with enough resolution, although these disc features do not necessarily confirm the presence of planets. The first indirect detection of planets at these wavelengths was achieved from detailed analyses of the gas kinematics in the HD 163296 disc (Pinte et al. 2018; Teague et al. 2018).

While these indirect detections with ALMA and other (sub)millimetre facilities tantalize evidence for young, and in some cases, massive planets in discs, the interpretation is not unique. A direct detection of young planet candidates is required to confirm their presence in discs. Additionally, a direct detection from the infrared (IR) and spectroscopy is crucial to further characterize the planet properties (e.g. its atmosphere). Several attempts have been made to directly detect young planet candidates in discs, by means of near- and mid-IR high-contrast imaging, but the vast majority of these efforts resulted in no detections. Testi et al. (2015) searched for planets in HL Tau in the *L* band, without any point sources detected but setting upper limits of planet masses at the rings' location. Much more stringent upper limits were set for the TW Hya system by Ruane et al. (2017) with the Keck/NIRC2 instrument, and for the HD 163296 system by Guidi et al. (2018). On a few occasions, point-like sources have been claimed as detections in other protoplanetary discs. Reggiani et al. (2014) and Quanz et al. (2015) announced direct evidence (as point sources) of protoplanets embedded in HD 169142 and HD 100546 in the *L* and M' bands, respectively, using the NaCo instrument at the Paranal Observatory of the European Southern Observatory. While apparently convincing, both detections have been disputed and further confirmation is still pending. More recently, an additional candidate, still requiring confirmation, has been detected by Reggiani et al. (2018) in the spiral arm of MWC 758 in the *L* band. To date, the most convincing direct detection of a young planet in a protoplanetary disc is the multiwavelength detection of PDS 70b, confirmed using multiple-epoch data (Keppler et al. 2018); the system also includes an additional planet, PDS 70c (Haffert et al. 2019).

Hydrodynamical (HD) simulations of planet–disc interactions have greatly improved our theoretical understanding of these systems. Kley (1999) and Bryden et al. (1999) simulated a planet embedded in a disc in two dimensions (2D), showing the formation of gaps from the planet–disc interaction and deriving crucial properties of protoplanetary discs as mass accretion and viscosity. Many other studies followed, focusing on the characterization of geometrical properties and the derivation of important disc evolution parameters (like the viscosity, e.g. Szulágyi et al. 2014). The implementation of nested grids alleviated the resolution limitation and computation times, allowing for the first 3D simulations to be performed (see D'Angelo, Kley & Henning 2003).

The detectability of a protoplanet at different wavelengths can also been inferred from HD simulations. Indeed, Wolf & D'Angelo (2005) performed mock observations to infer planet signatures that could be detected using ALMA, while Zhu (2015) focused on the detectability in IR bands of the circumplanetary disc (CPD) around highly accreting planets. Other indirect observable signatures due to the presence of planets have been also investigated: gap-opening effects at various wavelengths (e.g. Dong, Zhu & Whitney 2015a; Rosotti et al. 2016; Dipierro & Laibe 2017; Dong & Fung 2017; Jang-Condell 2017), disc inclination effects (Jang-Condell & Turner 2013), spiral arms in scattered light (Dong et al. 2015b; Fung & Dong 2015; Juhász et al. 2015; Juhász & Rosotti 2018), planet shadowing (Jang-Condell 2009), and even the effect of migrating planets (Meru et al. 2019; Nazari et al. 2019).

This study focuses on the early evolutionary stages, when the accretion of disc material on to the planet might still have an incidence on the total planet brightness. We performed 3D HD simulations, using high-resolution nested grids in the planet surroundings. Column densities and extinction coefficients at the planet location are derived from the simulations, in order to infer planet magnitudes in the *J*, *H*, *K*, *L*, *M,* and *N* bands. This model can be used to guide future direct imaging observations of young planets embedded in protoplanetary discs.

This work is organized as follows. In Section 2, we describe the simulations set-up and the model. The results of the different simulated systems are presented in Section 3. The application of the model to known protoplanetary discs is discussed in Section 4, and the main implications of this work are summarized in Section 5.

2 SET-UP AND MODEL DESCRIPTION

The HD simulations were performed with the PLUTO code (Mignone et al. 2010, 2012), a 3D grid code designed for astrophysical fluid dynamics. The details of the simulations' set-up, the description of the planet flux model used (Section 2.2), and the derivation of the expected planet magnitudes (Section 2.3) are presented in this section.

2.1 Simulation set-up

We modelled a gaseous disc in hydrostatic equilibrium around a central star with a protoplanet on a fixed orbit. The disc evolution is determined by the α-viscosity prescription (Shakura & Sunyaev 1973). The disc is considered to be locally isothermal, for which the equation of state (EoS) is described as

$$P = n\, k_{\rm B}\, T = \frac{\rho}{m_{\rm u}\,\mu}\, k_{\rm B}\, T, \tag{1}$$

where P is the pressure, n is the total particle number density, $k_{\rm B}$ is the Boltzmann constant, T is the temperature, ρ is the gas density, $m_{\rm u}$ is the atomic mass unit, and μ is the mean molecular weight. The temperature in the disc varies only radially:

$$T(R) = T_0 \left(\frac{R}{R_0}\right)^q \tag{2}$$

with R being the radius in cylindrical coordinates, $R_0 = 5.2$ au, $T_0 = 121$ K, and q the temperature exponent factor, set to -1. The adopted density distribution of the protoplanetary disc (as in Nelson, Gressel & Umurhan 2013) is described as

$$\rho(r,\theta) = \rho_0 \left(\frac{R}{R_0}\right)^p \exp\left[\frac{GM_\star}{c_{\rm iso}^2}\left(\frac{1}{r}-\frac{1}{R}\right)\right], \tag{3}$$

where r refers to the radial distance from the centre in spherical coordinates, θ is the polar angle [thus, $R = r\cos(\theta)$], ρ_0 is the

density at the planet location, p is the density exponent factor, in our case with value -1.5, G is the universal gravitational constant, $M_\star$ is the mass of the central star, and $c_{\rm iso}$ is the isothermal speed of sound. From this equation, the surface density Σ scales radially as

$$\Sigma(R) = \Sigma_0 \left(\frac{R}{R_0}\right)^{-p'} \tag{4}$$

with a power law with index $p' = -0,5$. The planet is included as a modification in the gravitational potential of the central star in the vicinity of the planet location, which is kept fixed. The gravitational potential ϕ considered in the simulations is

$$\phi = \phi_\star + \phi_{\rm pl} + \phi_{\rm ind}, \tag{5}$$

where $\phi_\star$ is the term due to the star, $\phi_{\rm pl}$ the planet potential, and $\phi_{\rm ind}$ accounts for the effect of the planet potential on the central star. In the cells closest to the planet (cells at a distance to the planet lower that the smoothing length $d_{\rm rsm}$), $\phi_{\rm pl}$ is introduced with a cubic expansion as in Klahr & Kley (2006) to avoid singularities at the planet location:

$$\phi_{\rm pl}(d < d_{\rm rsm}) = -\frac{GM_{\rm pl}}{d}\left[\left(\frac{d}{d_{\rm rsm}}\right)^4 - 2\left(\frac{d}{d_{\rm rsm}}\right)^3 + 2\left(\frac{d}{d_{\rm rsm}}\right)\right] \tag{6}$$

with d referring to the distance between the cell and planet. We set $d_{\rm rsm}$ to be $0.1R_{\rm Hill}$ in the first four simulations. In two additional runs, we decreased this value and doubled the grid resolution in order to investigate the behaviour of the density in the cells close to the planet surface. In Table 1, all the values of $d_{\rm rsm}$ used in the simulations are shown.

The gas rotational speed (Ω) is sub-Keplerian; the additional terms arise from the force balance equations in radial and vertical directions (see e.g. Nelson et al. 2013). It is described by

$$\Omega(R, z) = \Omega_{\rm K}\left[(p+q)\left(\frac{h}{R}\right)^2 + (1+q) - \frac{qR}{\sqrt{R^2+z^2}}\right]^{1/2} \tag{7}$$

with z being the vertical coordinate, $\Omega_{\rm K}$ the Keplerian orbital speed, and h the vertical scale height of the disc.

The simulated protoplanetary discs had a stellar mass of 1.6 $M_\odot$ and a surface density at 5.2 au of 127 g cm^{-2}, consistent with estimates of the minimum-mass solar nebula (Hayashi 1981) and the densest discs in the star-forming regions in the solar neighbourhood. (Andrews 2015; Tazzari et al. 2017). The model can be adapted to systems with different characteristics by rescaling our results to different surface densities and other parameters, as discussed in Section 4.

We modelled three different planetary masses (1, 2, and 5$M_{\rm J}$) embedded in a viscous disc with $\alpha = 0.003$. A fourth inviscid run with mass 1$M_{\rm J}$ was performed in order to study the effect of viscosity on planet detectability, since recent studies with non-ideal magnetohydrodynamical effects have shown that the disc can be laminar at the mid-plane (Paardekooper 2017). Besides, two additional runs with doubled grid resolution were done for the 1 and 5$M_{\rm J}$ cases, in order to improve our understanding of the disc–planet interaction at the upper atmospheric layers of the planet. In total, six simulations were carried out, as summarized in Table 1. During the first 20 orbits, the planetary mass was raised until its final value (1, 2, or 5$M_{\rm J}$) following a sinusoidal function, in order to prevent strong disturbances in the disc. The simulations ran for 200 orbits, once a steady state of the system is reached.

The resolution in the vicinity of the planet is crucial for our study in order to obtain realistic IR optical depths due to the disc material close to the planet surface. To fulfil this, we used a three-level nested grid with a maximum resolution of $0.02R_{\rm Hill}$. For the 1, 2, and 5$M_{\rm J}$ planets, and considering planetary radii of 1.74, 1.69, and 1.87$R_{\rm J}$ from the 1-Myr-old *hot-start* models of Spiegel & Burrows (2012) (details of these models given in Section 2.2), the maximum resolution corresponds to 7.3, 9.5, and 11.8 planetary radii, respectively. In the two additional runs with doubled resolution over the entire grid, the smallest cell size was set to $0.01R_{\rm Hill}$. To test the accuracy of our simulations, we inspected the gas streamlines in the vicinity of the planet (Section 3.1.3). The grid is centred at the star location; thus, close to the planet, the grid appears to be Cartesian. As suggested by Ormel, Kuiper & Shi (2015a) and Ormel, Shi & Kuiper (2015b), the grid describes the CPD correctly if the gas streamlines form enclosed circular orbits around the planet location, which is confirmed in our simulations (Fig. 1).

To save computational time, we assumed the disc to be symmetric with respect to the mid-plane. The simulated range for θ goes from the mid-plane up to 7°, adequate for a proper representation of the disc dynamics and the column density derivation. At the disc upper layers, density has decreased more than or equal to two orders of magnitude, and the contribution to the column densities of these upper layers is negligible. The details for the three grid regions are summarized in Table 2.

2.2 Intrinsic, accretion, and total planet fluxes

The total planet emission is considered as a combination of its intrinsic and accretion flux components. At the wavelengths studied, the intrinsic flux of the planet is expected to dominate, except in those cases with very high accretion rates, on to the planet.

The intrinsic component of the planet flux is derived from the evolutionary models of Spiegel & Burrows (2012). These models provide the absolute magnitudes in the J, H, K, L, M, and N IR bands for a range of planet masses and as a function of age, up to 100 Myr. Following their nomenclature, we refer to *hot-start* and *cold-start* models as the cases of a planet fully formed via disc instability or via core accretion, respectively. In a more realistic scenario, a planet would be characterized by an intermediate solution.

The total accretion luminosity is given by (Frank, King & Raine 1985)

$$L_{\rm acc} \simeq \frac{GM_{\rm pl}\dot{M}_{\rm acc}}{R_{\rm acc}}, \tag{8}$$

where $M_{\rm pl}$ is the planetary mass, $\dot{M}_{\rm acc}$ is the mass accretion rate on to the planet, and $R_{\rm acc}$ is the accretion radius, the distance to the planet at which accretion shocks occur (Hartmann 1998). $R_{\rm acc}$ is typically two to four times the planetary radius; we have chosen $R_{\rm acc} \equiv 4R_{\rm pl}$ for the estimation of the accretion luminosity. The accretion shocks are not resolved in the simulations; this is out of the scope of this work. Nevertheless, the computation of $\dot{M}_{\rm acc}$ from the simulations (explained in the last paragraph of this section) is independent of $R_{\rm acc}$. The accretion flux considered in this model accounts only for the accretion shocks' irradiation. The flux irradiated by the CPD is not taken into account.

The continuum emission of the accretion shocks is at temperatures ($\equiv T_{\rm acc}$) of the order of $\sim 10^4$ K (Hartmann, Herczeg & Calvet 2016). To obtain the accretion flux in each band, we approximate the shocks' emission to a blackbody (Mendigutía et al. 2011) that emits at a radius $R_{\rm acc}$. The surface area covered by the shocks is a fraction (defined as $b_{\rm acc}$) of the spherical surface with the same radius. In this model, the accretion flux in a given band ($F_{\rm acc}^{\rm band}$) is computed as a fraction $b_{\rm acc}$ of the flux within the same band of a

Table 1. Set-up parameters of the simulations and inferred column mass densities σ. The disc aspect ratio H, defined as $H = h/R$, was set to 0.05 in all the simulations. The columns refer to the α-viscosity parameter for a viscously evolving disc; cell size in the vicinity of the planet, given in Hill radii ($R_{\rm Hill}$) and in planet radii ($R_{\rm pl}$); smoothing and accretion radii; and predicted column mass densities in g cm^{-2}. σ is obtained by integrating over every cell above the planet except the cells within $d_{\rm rsm}$. The uncertainty is computed from the dispersion of the σ value in the last 10 orbits. Planet radii are taken from the evolutionary models of giant planets of Spiegel & Burrows (2012).

Run	α	Cell size ($R_{\rm Hill}$)	Cell size ($R_{\rm pl}$)	$d_{\rm rsm}$ ($R_{\rm Hill}$)	$r_{\rm sink}$ ($R_{\rm Hill}$)	σ
$1M_{\rm J}$	0.003	0.02	7.3	0.10	0.07	2.8 $\pm$ 0.9
$2M_{\rm J}$	0.003	0.02	9.5	0.10	0.07	0.8 $\pm$ 0.6
$5M_{\rm J}$	0.003	0.02	11.8	0.10	0.07	0.011 $\pm$ 0.007
$1M_{\rm J}$, inviscid disc	$\sim$0	0.02	7.3	0.10	0.07	1.2 $\pm$ 0.3
$1M_{\rm J}$, doubled resolution	0.003	0.01	3.7	0.03	0.03	2.7 $\pm$ 1.2
$5M_{\rm J}$, doubled resolution	0.003	0.01	5.9	0.04-0.05	0.03	0.01 $\pm$ 0.01

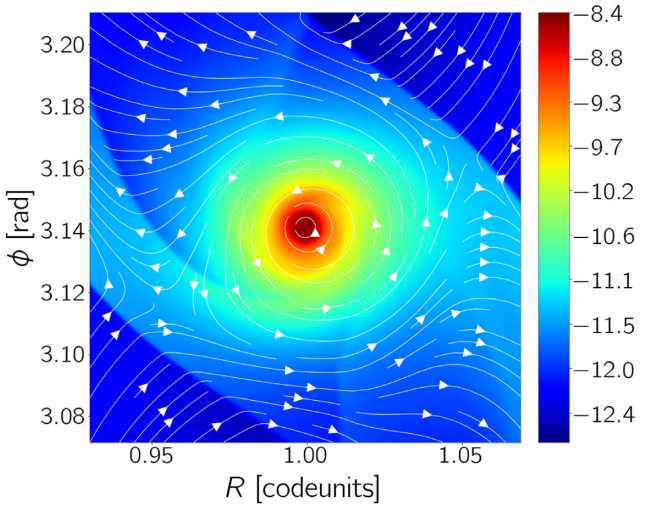

Figure 1. Density map at the mid-plane near a $1M_J$ planet. The gas streamlines are plotted on top, showing the circular motion of the gas around the planet. A value of 1 in radial code units is equivalent to 5.2 au. The colour scale shows the logarithm of the density, in g cm^{-3}.

spherical blackbody ($F_{\rm bb}^{\rm band}$) with temperature $T_{\rm acc}$ and radius $R_{\rm acc}$:

$$F_{\rm acc}^{\rm band} = b_{\rm acc}\, F_{\rm bb}^{\rm band}. \tag{9}$$

The factor $b_{\rm acc}$ can be estimated as the fraction between the total accretion luminosity $L_{\rm acc}$ (from equation 8) and the bolometric luminosity of the same blackbody:

$$b_{\rm acc} = \frac{L_{\rm acc}^{\rm tot}}{L_{\rm bb}^{\rm tot}}. \tag{10}$$

We tested various values of $T_{\rm acc}$; the results shown along this work are obtained using a shock temperature of 20 000 K. As discussed, for the band flux results (Section 3.2.1), assuming lower $T_{\rm acc}$ does not vary the flux results significantly.

The gas accretion on to the planet is modelled following the prescription in Kley (1999), and also Dürmann & Kley (2015). At each time-step, a fraction $f_{\rm acc}\ \Delta t\ \Omega$ of the gas is removed from the cells enclosed by a sphere of radius $r_{\rm sink}$ centred at the planet (values for $r_{\rm sink}$ given in Table 1). This method mimics the direct accretion on to the planet surface. The values of $r_{\rm sink}$ have been chosen to guarantee convergence; as shown in Tanigawa & Watanabe (2002), the estimated accretion rates converge to a stable value if $r_{\rm sink} \lesssim 0.07 R_{\rm Hill}$. This is independent of the $f_{\rm acc}$ value, which is set to 1. The mass accreted is removed from the computational domain instead of being added to the planet mass (accreted mass is negligible compared to the total planet mass, about 10^{-5} times lower).

2.3 Derivation of expected magnitudes

The extinction in our model is due to the disc material around the planet. We assume that there are no additional astronomical objects of significant brightness or size between the studied planet and the observer. The extinction in the V band is derived from the column mass density obtained from the simulations. Using the magnitude–flux conversion formula from Güver & Özel (2009), assuming a constant gas-to-dust ratio of 100, and a molecular weight of 2.353, we have

$$A_V\ ({\rm mag}) = \frac{N_{\rm H}\ ({\rm atoms\ cm^{-2}})}{2.2 \times 10^{21}\ ({\rm atoms\ cm^{-2}\ mag^{-1}})}. \tag{11}$$

The above relation was inferred from observations, and it applies to an averaged interstellar medium (ISM) in the Milky Way. While the gas-to-dust ratio used is a good first approximation, variations may be expected, particularly in the vicinity of the planet. Recent surveys in close star-forming regions indicate that this ratio might indeed be different in many discs (Miotello et al. 2017).

From the inferred A_V, the extinction coefficients ($A_{\rm band}$) and optical depths ($\tau_{\rm band}$) are obtained using the diffuse ISM extinction curves of Cardelli, Clayton & Mathis (1989) for the J, H, and K bands and of Chiar & Tielens (2006) (which accounts for the silicate feature around 10 μm) for the L, M, and N bands. The expected fluxes are then given by

$$F_{\rm expected}^{\rm band} = F_{\rm pl}^{\rm band}\, {\rm e}^{-\tau_{\rm band}} \tag{12}$$

with $F_{\rm pl}^{\rm band}$ being the total planet flux in that band. The resulting $F_{\rm expected}^{\rm band}$ is the expected band flux that we would observe for a planet embedded in a protoplanetary disc with an ongoing accretion on to the planet.

3 MODEL RESULTS

In this section, we first present the results from the HD simulations (Section 3.1), followed by the results from our model (Section 3.2)

3.1 Results from the HD simulations

Jupiter-sized planets embedded in a disc generally carve a gap after several orbits (Bryden et al. 1999). In our simulations, this can be seen in 2D density maps of the disc as a function of time (Fig. 2, for the $1M_J$ case). For more massive planets, the gap carving process is faster, as one would expect from planet formation theory.

Table 2. Resolution and extension (as # of cells) for each coordinate (radial distance R, polar θ and azimuthal ϕ angles) of our three-level grid. There is no low-resolution level for the θ coordinate.

	Level 1 (*hi-res*)		Level 2 (*mid-res*)		Level 3 (*low-res*)
Coordinates	Resolution	# of cells	Resolution	# of cells	# of cells
R	$0.02R_{\rm Hill}$	128	$0.08R_{\rm Hill}$	64	128
θ	$0.02R_{\rm Hill}$	64	$0.08R_{\rm Hill}$	32	–
ϕ	$0.02R_{\rm Hill}$	128	$0.08R_{\rm Hill}$	128	128

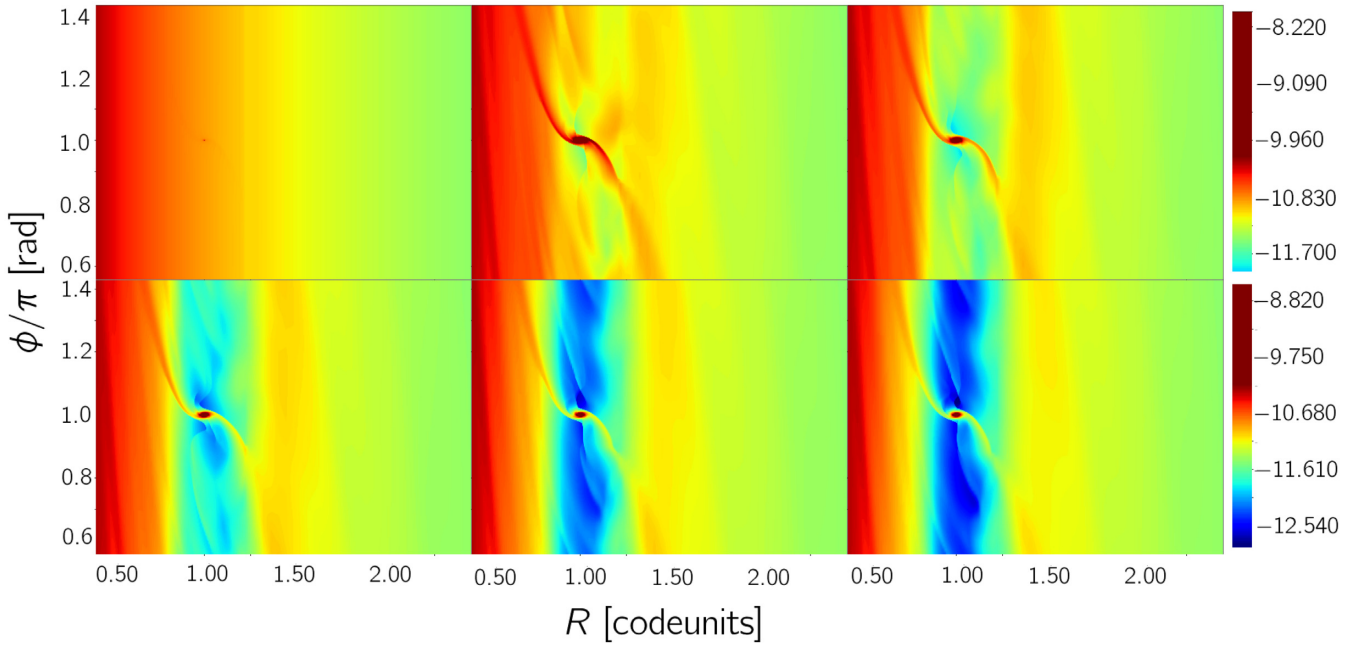

Figure 2. Evolution in time of the 2D density map at the mid-plane for the viscous disc with an embedded $1M_{\rm J}$ planet. A value of 1 in radial code units is equivalent to 5.2 au (Jupiter semimajor axis). Density is represented in a logarithmic scale, with values in g cm^{-3}. From the top left-hand side to bottom right-hand side, each snapshot represents the density ρ of the disc after 1, 20, 50, 100, 150, and 200 orbits.

The gap opened by each planet can be compared to disc models to verify the quality of our simulations. We tested our resulting surface density profiles with an analytical model for gaps in protoplanetary discs, as described in Duffell (2015). An algebraic solution of the gap profiles is presented in that work, together with the derivation of a formula for the gap depth. In Fig. 3, we show the azimuthally averaged surface density radial profiles relative to the unperturbed surface density (Σ_0) for the 1, 2, and $5M_{\rm J}$ simulated planets in a viscous disc. The solid lines represent the profiles after a steady state is reached, and the dashed lines denote the surface density after the first 20 orbits. The predicted gap depths from the model (Duffell 2015, equation 9) are shown in the figure as horizontal dash–dotted lines.

Our results for 1 and $2M_{\rm J}$ planets are in very good agreement with the analytical model. The gap for a $5M_{\rm J}$ planet is relatively deeper than the prediction from the model. Nevertheless, the model by Duffell (2015) fails at reproducing the gap profile produced by planets with very high masses, as discussed in that work. Therefore, we can trust the quality of our simulations from the concordance at low planet masses with analytical models.

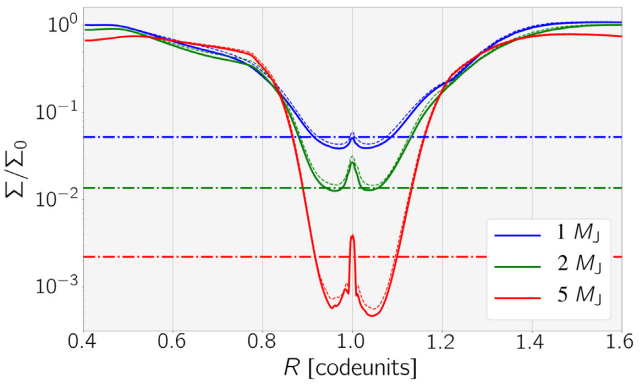

Figure 3. Surface density radial profile for 1, 2, and $5M_{\rm J}$ planets after the simulations reach a steady state, shown as solid lines. The dash–dotted lines are the respective predicted gap-depths, derived from an analytical model for gaps in protoplanetary discs (Duffell 2015). The dashed lines represent the surface density after 20 orbits. A value of 1 in radial code units is equivalent to 5.2 au.

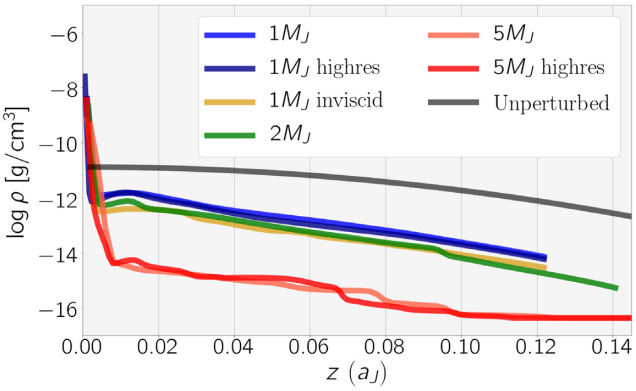

Figure 4. Vertical density above the planet for each simulation. The horizontal axis represents the height from the mid-plane in the Jupiter semimajor axis (a_J) and the vertical axis shows the density in a logarithmic scale, in g cm^{-3}.

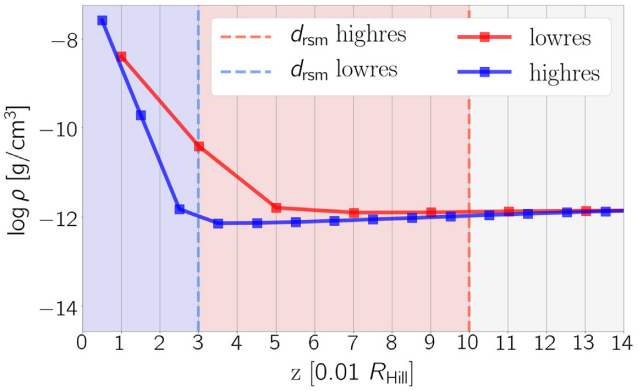

Figure 5. Vertical density profile close to the $1M_J$ planet, comparing the doubled-resolution case (blue line) to the original case (red). The vertical grid spacing is $0.01R_{Hill}$, equivalent to the cell size for the doubled-resolution run, and half the cell size for the original run. The red and blue dashed lines represent the smoothing radii for the original and the new runs, respectively.

3.1.1 *Column mass density*

The column density is obtained by integrating the disc density over the line of sight towards the planet. We considered our system to be face-on, since it is the most likely geometry for a direct protoplanet detection. The density above the planet for every simulation is shown in Fig. 4, together with the unperturbed (initial) density. The highest densities correspond to the $1M_J$ simulation. For more massive planets, the disc densities are lower, since the planet carves a deeper gap. In the inviscid case, the carved gap cannot be refilled with adjacent material, resulting in lower densities compared to the viscously evolving case.

The planet and its atmosphere are not resolved in these simulations; therefore, the first cell is assumed to be the planet outer radius. The sharp peak from the vertical density profiles extends over the first two to three cells. This is expected to be a combination of several effects, mainly an artefact of the simulations due to the potential smoothing (equation 6), which affects every cell within d_{rsm}. However, we cannot exclude the possibility that a fraction of the peak might also be the real density stratification of the material at the layers closest to the planet. Additionally, this overdensity is also altered by the accretion radius (see Section 2.2), and limited by the grid resolution. A fully resolved CPD would be necessary to disentangle between the different causes. However, we tested whether the extension of the peak is an artefact due to the potential softening and the mentioned resolution limitations. To this aim, we performed two additional simulations with doubled resolution over the entire grid. We also decreased both accretion and smoothing radii to 0.03–$0.05R_{Hill}$. The values of the main parameters for the doubled resolution runs are summarized in Table 1. This test was done for the discs with 1 and $5M_J$ planets. The grids from the last snapshot of the original simulations were readjusted to the new resolution, and we let the system evolve until a new steady state was reached ($\leq$15 orbits needed in both cases). The vertical density at the closest cells above the planet for both original and doubled resolutions for the $1M_J$ case is shown in Fig. 5. The vertical grid lines represent $0.01R_{Hill}$, and the coloured lines illustrate the d_{rsm} in both original and doubled-resolution runs. The figure shows that the overdensity with doubled resolution spans approximately half the original case. This is in accordance with what we expect if the overdensity is due to the smoothing within d_{rsm}. If we were able to completely remove the potential smoothing, we would see a peak only inside the planet radius, i.e. within the first cell.

Table 3. Mass accretion rates and bolometric fluxes for every simulated system. Fluxes are expressed in W m^{-2}.

M_{pl}	$\dot{M}_{acc}$(M$_\odot$ yr^{-1})	F_{intr}^{Hot}	F_{acc}^{Hot}	F_{intr}^{Cold}	F_{acc}^{Cold}
$1M_J$	5.7e−8	2.8e4	1.7e5	4.8e3	3.2e5
$2M_J$	6.8e−8	1.2e5	4.3e5	8.9e3	9.3e5
$5M_J$	2.8e−8	7.4e5	3.3e5	1.2e4	1.1e6
$1M_J$ inviscid	1.0e−8	2.8e4	3.0e4	4.8e3	5.6e4

From the results of this test, we consider the column mass density σ as the integrated density for all the cells above the smoothing radius. The resulting σ for each of the simulated systems are included in Table 1. The uncertainty considered is the dispersion of the column mass density for the last 10 orbits of each simulation. The predicted magnitudes for 1 and $5M_J$ planets are derived using the σ values from the doubled-resolution runs, since in these cases the planet–disc interaction is represented more accurately. The values for the original- and doubled-resolution cases are within their respective uncertainty: For a $1M_J$ run, we obtained 2.8 ± 0.9 and 2.7 ± 1.2 g cm^{-2}, while for the $5M_J$ runs, the column mass densities were 0.011 ± 0.007 and 0.01 ± 0.01 g cm^{-2}, respectively.

3.1.2 *Mass accretion rates*

The prescription used to derive the mass accretion rates from the simulations has been described in Section 2.2. The final value of $\dot{M}_{acc}$ for each simulated planet is the optimal value of parameter c when fitting the evolution of $\dot{M}_{acc}$ in the last 50 orbits by an exponential function defined as $f(x) = a\,e^{-bx} + c$. The resulting accretion rates are of the order of 10^{-8} M$_\odot$ yr^{-1}, summarized in Table 3. The highest $\dot{M}_{acc}$ is obtained for a system with a $2M_J$ planet. This is somewhat counterintuitive, as one may expect the least massive planet to have the lowest accretion rate, and the most massive planet to have the highest. There are two effects to be considered: the viscosity that refills the gap and the gravitational force of the planet. A more massive planet creates a stronger gravitational potential, a larger CPD, and has a larger accretion rate, while, on the other hand, if the disc evolves viscously, it can replenish the accreted material with new material, thus keeping a higher $\dot{M}_{acc}$ value. Beyond a certain planet mass, the gravitational potential clears large regions quicker, which limits the refill of the

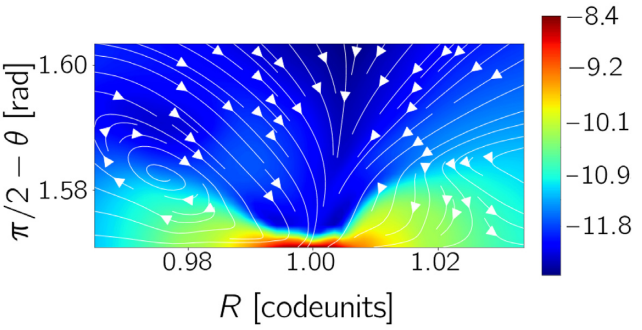

Figure 6. Edge-on-view density map with gas streamlines around the planet. An important part of the gas is being accreted vertically. A value of 1 in radial code units is equivalent to 5.2 au. The scale represents the logarithm of the density, in g cm^{-3}.

gap material, thus ultimately reducing the $\dot{M}_{\rm acc}$. Our results indicate that the mass of the planet for which this occurs is between 2 and 5$M_{\rm J}$. The different accretion rates obtained for the 1$M_{\rm J}$ planet in a viscous and an inviscid disc can be understood by considering that an inviscid disc cannot replenish the gap opened by a planet, and, consequently, there is less material to feed the CPD.

Care should be taken when considering these results because of the limitations posed by isothermal simulations, which do not account for accretion heating in the vicinity of the planet. This results in an overestimation of the accretion rate. These simulations provide an upper limit of the expected accretion rates, and this should be taken into account when the model is applied to real systems.

3.1.3 Gas streamlines

Gas streamlines provide useful insights into the disc behaviour and the planet–disc interaction. In the close-up top view of the system (Fig. 1), the gas streamlines at the system mid-plane are plotted as vectors. As expected from the accretion models, a CPD is formed and the gas motion is concentric to the planet. The gas streamlines follow closed trajectories in the regions nearest to the planet, which indicates that the grid does describe the accreting planet with a CPD accurately (as discussed in Ormel et al. 2015a).

Accretion on to the planet occurs not only in the orbital plane from the CPD but also vertically (see e.g. Szulágyi et al. 2016). In our simulated systems, the gas is indeed falling on to the planet from its pole or with a small inclination angle from the vertical. Fig. 6 shows that a high fraction of the material is being accreted vertically on to the 1$M_{\rm J}$ planet.

3.2 Predicted planet magnitudes

3.2.1 Bolometric and band fluxes

Accretion and intrinsic bolometric fluxes for each planet considered in this work are shown in Table 3. Mass accretion rates are also included in the table. The difference in $F_{\rm acc}$ between *hot-* and *cold-start* models arises from the different planet radius $R_{\rm pl}$ of each model (taken from Spiegel & Burrows 2012), since the $R_{\rm acc}$ used to compute the accretion flux (equation 8) is assumed to be $\equiv 4R_{\rm pl}$. The bolometric accretion flux is higher than the planet's intrinsic flux for all cases. Nevertheless, the accretion flux (which peaks at 0.15 μm, with $T_{\rm eff} \sim 20\,000$ K) is in most cases lower in the IR bands considered than the intrinsic planet flux, whose spectrum peaks in the IR (∼1–10 μm). This can be seen in the left-hand panel of Fig. 7. The figure shows the accretion and intrinsic fluxes of planets with masses 1, 2, and 5$M_{\rm J}$ for *hot-* and *cold-start* planet models. Intrinsic fluxes are considerably lower for *cold-start* planets than for the *hot-start* models. The accretion contribution can be significant, especially in the *cold-start* cases in the *J*, *H*, *K,* and *L* bands. Reducing the $T_{\rm acc}$ shifts the accretion maximum to longer wavelengths, but it highly decreases its bolometric value, and, consequently, the overall picture does not vary significantly.

These results indicate that the radiation from accretion shocks near the planet is an important factor of the planet flux. Nevertheless, it is worth keeping in mind that these results are for accretion rates inferred from isothermal simulations, which are generally overestimated. For more realistic accretion rates at this stage (∼10^{-10} M$_\odot$ yr^{-1}), intrinsic flux dominates at these wavelengths. When scaling our models to larger distances from the host star, accretion rates are highly reduced due to the scaling for lower disc densities. Consequently, intrinsic fluxes dominate in planets farther out in the disc for both *hot-* and *cold-start* scenarios.

3.2.2 Extinction coefficients and predicted magnitudes

From the column mass densities, we derived extinction coefficients for each planet in the *J*, *H*, *K*, *L*, *M,* and *N* bands. The inferred coefficients are included in Table 4, and plotted in the top left-hand panel in Fig. 8. Extinction coefficients at wavelengths $\lesssim$ 2 μm are extremely high for 1 and 2$M_{\rm J}$. The effect of extinction decreases for longer wavelengths, but it rises up again at ∼8–12 μm due to the silicate feature present in the diffuse ISM. For a 5$M_{\rm J}$ planet, extinction coefficients are very low in every IR band. This is due to its ability to open a gap in the disc very effectively, and, consequently, the disc density around the planet and the inferred column density are very low.

The derived magnitudes for each simulated planet as a function of wavelength are shown in the top right-hand panel in Fig. 8. For each planet, the upper and lower curves represent its *hot* and *cold* models. The results include the extinction from the disc material and radiation from the accretion shocks near the planet. The magnitudes for every IR band and planet at 5.2 au are summarized in Table 4. For each simulated planet, the rows in the table show the absolute magnitude of the planet, including the contribution from accretion; the extinction coefficients due to the disc material; and the predicted absolute magnitude, including extinction effects.

The predicted magnitudes for a given planet decrease as a function of wavelength, except at $\sim$ 10 μm due to the silicate feature in dust grain opacities. The curves are more flattened for more massive planets. This is due to the more efficient depletion of material in the planet vicinity, which yields lower column densities, hence lower extinction. For the most massive planet considered (5$M_{\rm J}$), the gap clearing is extremely effective and extinction in any IR band is negligible. In the inviscid scenario with a 1$M_{\rm J}$, the gap cannot be replenished efficiently compared to the viscously evolving case. This results in a gap with a lower density and extinction. At $\lesssim$2 μm, 1–2$M_{\rm J}$ planets are completely obscured by the disc material (with extinction above 30 and 15 mag, respectively). These results are obtained for an unperturbed surface density of $\Sigma = 127$ g cm^{-2} at 5.2 au.

We have used the ISM law to estimate the extinction under the assumption that mostly small grains are present in the disc

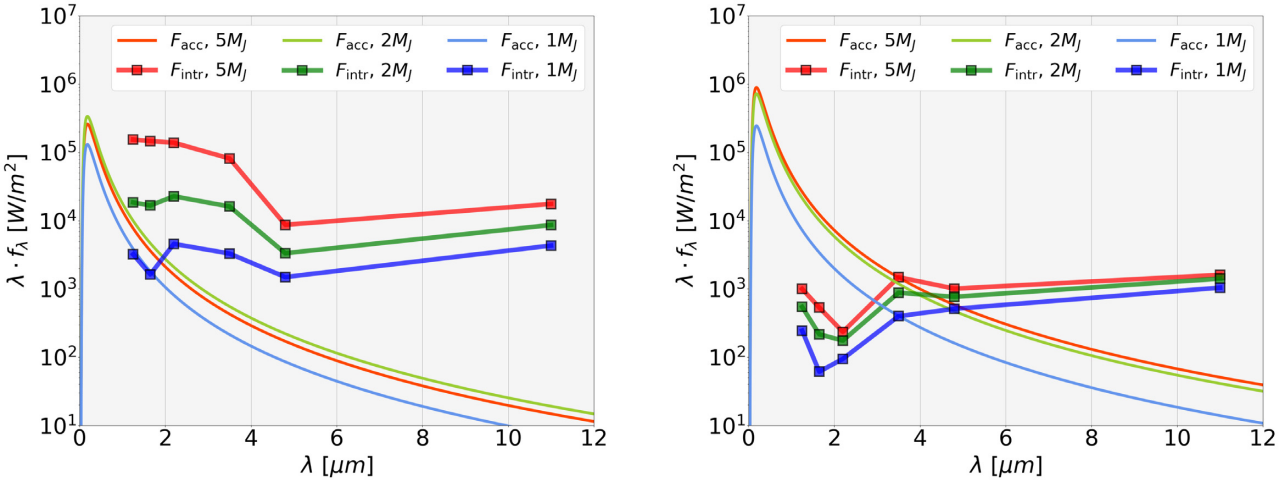

Figure 7. Intrinsic (F_{intr}) and accretion fluxes (F_{acc}) for 1, 2, and $5M_J$ planets. The results for planets with a *hot-start* model are shown in the left-hand panel, while *cold-start* models are shown in the right-hand panel. The intrinsic fluxes are plotted at the central wavelength of each band.

Table 4. Absolute magnitudes for planets at 5.2 au to the host star, with masses $1M_J$ – viscous and inviscid scenarios – $2M_J$, and $5M_J$. Mag_{pl} is the total magnitude of the planet, including accretion flux; A_{band} is the extinction coefficient in each band; and $Mag_{expected}$ is the magnitude of the planet considering extinction due to disc material. All values are in mag.

		Hot-start planet						*Cold-start* planet					
		J	*H*	*K*	*L*	*M*	*N*	*J*	*H*	*K*	*L*	*M*	*N*
$1M_J$	Mag_{pl}	13.74	13.75	12.92	12.40	11.33	10.00	13.72	13.81	13.84	13.56	12.65	11.88
	A_{band}	91.32	58.41	36.75	19.96	15.63	28.15	91.32	58.41	36.75	19.96	15.63	28.15
	$Mag_{expected}$	105.07	72.16	49.67	32.36	26.96	38.16	105.04	72.21	50.59	33.52	28.28	40.04
$2M_J$	Mag_{pl}	12.58	12.22	11.44	10.87	10.51	9.31	12.72	12.80	12.84	12.60	12.10	11.58
	A_{band}	26.33	16.84	10.60	5.84	4.57	8.24	26.33	16.84	10.60	5.84	4.57	8.24
	$Mag_{expected}$	38.91	29.06	22.04	16.71	15.08	17.55	39.06	29.65	23.44	18.44	16.67	19.81
$5M_J$	Mag_{pl}	11.09	10.21	9.48	9.00	9.29	8.33	12.61	12.69	12.73	11.88	11.62	11.34
	A_{band}	0.36	0.23	0.15	0.08	0.06	0.11	0.36	0.23	0.15	0.08	0.06	0.11
	$Mag_{expected}$	11.45	10.45	9.63	9.08	9.35	8.45	12.97	12.92	12.88	11.96	11.68	11.45
$1M_{inviscid}$	Mag_{pl}	14.98	14.83	13.28	12.63	11.39	10.02	15.56	15.66	15.62	14.79	12.95	12.00
	A_{band}	39.40	25.20	15.86	8.74	6.84	12.32	39.40	25.20	15.86	8.74	6.84	12.32
	$Mag_{expected}$	54.38	40.03	29.14	21.37	18.24	22.35	54.96	40.86	31.48	23.52	19.79	24.33

atmosphere above the planet. The actual value of extinction depends on the assumption on the dust properties. To investigate the implications of our assumption, we evaluated the impact of using different assumptions on the dust composition and size distributions. The results for the $1M_J$ viscously evolving case are shown in the bottom panels of Fig. 8. Two other dust models were investigated: one model of grains with fractional abundances comparable to that expected in protoplanetary discs mid-plane (Pollack et al. 1994) and a grain population with number density $n(a) \propto a^{-3.5}$ (where a is the grain size) between $0.01 < a < 1$ μm (Tazzari et al. 2016, for details), and a dust coagulation model for ice-coated silicate–graphite aggregates (type II grain mixing, see Ormel et al. 2009, 2011), applicable to the dust in protoplanetary discs (extinction shown is for grain sizes $a \sim 1$ μm). The results of the ice-silicate graphite model are in very good agreement with the ISM extinction used (in the *M* and *N* bands, the diffuse ISM extinction becomes larger). The other model provides similar results in the *J* and *H* bands; however, for longer wavelengths, extinctions are approximately two to three times larger than that for the diffuse ISM. Thus, when considering dust with different properties (e.g. composition, size, level of processing), the resulting predicted planet magnitudes might change due to the opacity variations in IR wavelengths.

On the other hand, the extinction is obtained assuming a gas-to-dust ratio of 100 along the disc. In the atmospheric layers of the disc above the planet, this ratio might be larger due to dust processing and settling. In this regard, our analysis provides a conservative estimate of extinction, and the presented results can be interpreted as the worst case scenario.

3.2.3 *Scaling results*

The simulations performed in this work are locally isothermal; therefore, the results can be scaled to account for different disc densities without altering the dynamics of the disc. We rescaled column mass densities and accretion rates for different planet positions and disc densities. The normalization of the surface density is readjusted in order to preserve the surface density profile $\Sigma(R)$ as in equation (4). In this way, we could extend the results of our model to study different systems. From dimensional analysis, the column

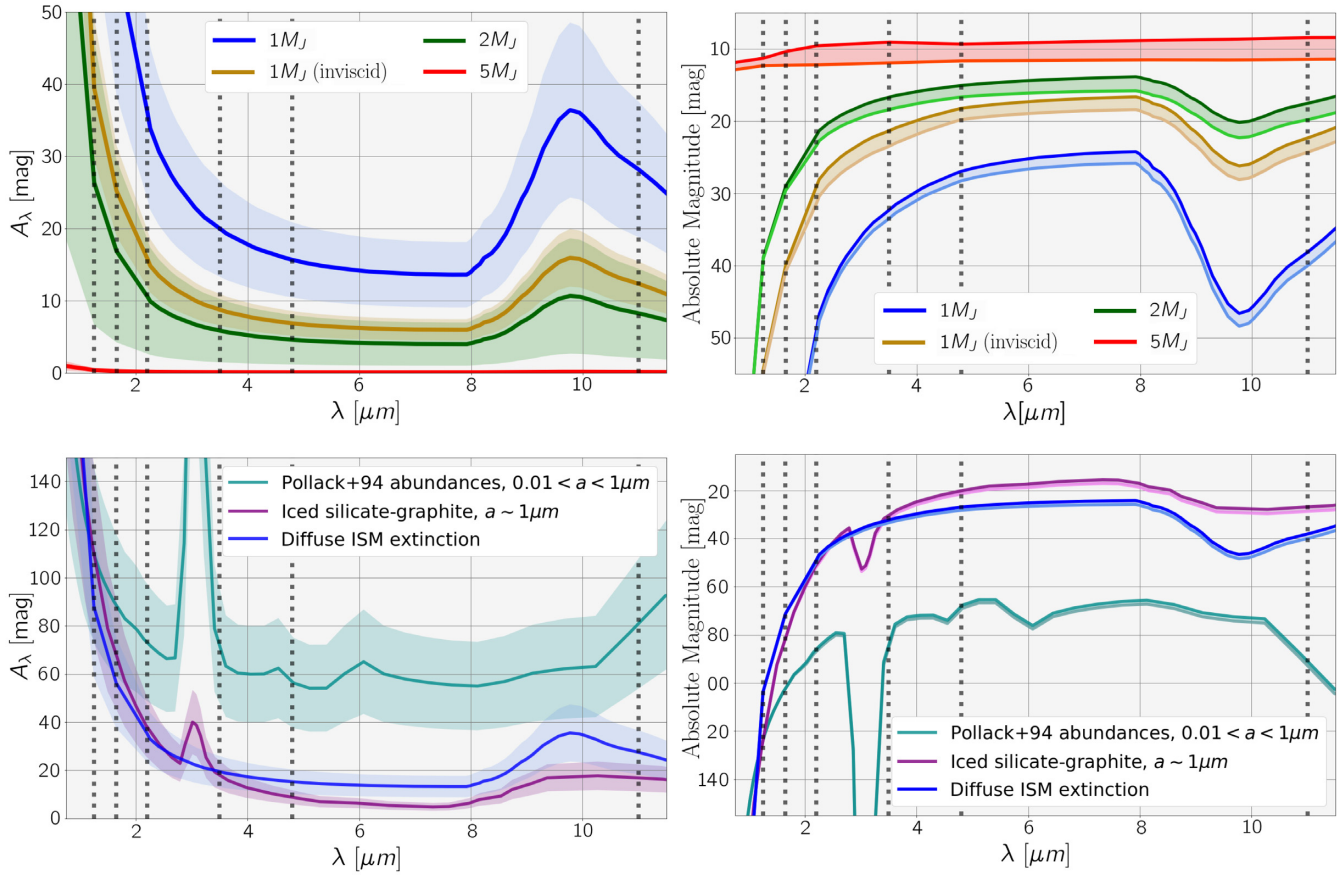

Figure 8. Top panels: extinction coefficients with uncertainties (left-hand side) and predicted magnitudes for the simulated systems (right-hand side), both as a function of wavelength. The predicted planet magnitudes are shown as an area delimited by the *hot* and *cold* planetary models. Bottom panels: extinction and predicted magnitudes of the $1M_J$ viscous case using different dust grain models. The results for the various dust models are normalized at A_V. For every panel, the vertical dotted lines represent (from the left- to right-hand side) the central wavelength of the *J*, *H*, *K*, *L*, *M*, and *N* bands.

mass density σ is directly proportional to the surface density, while the accretion rate $\dot{M}_{\rm acc}$ is proportional to the density and inversely proportional to orbital time. Surface density Σ decreases as $R^{-0.5}$ (equation 4), while the density at the planet location $\rho \propto R^{-1.5}$ (equation 3). These relationships are used to derive the scaling factors for σ and $\dot{M}_{\rm acc}$ for planets at a distance $\neq 5.2$ au. In case of renormalizing the surface density (as done for real systems in Section 4), the ratio between the unperturbed new and original surface densities at a fiducial distance multiplies the scaling factors of the column mass density and the mass accretion rate.

Scaling the distance to the central star would change the temperature at the planet location. While this has no *direct* impact on the scaling applied to the $\dot{M}_{\rm acc}$ obtained from the simulations (which has no explicit dependence on temperature), it would also change the disc aspect ratio $H = h/R$ since discs are generally flared. This would have an *indirect* effect on $\dot{M}_{\rm acc}$. In addition, the disc aspect ratio also determines the gap-opening planet mass and therefore the depth of the gap. We neglect these effects and remark that this is a limitation of our approach; the performed scaling provides a valuable understanding of how the planet location influences accretion rates and densities, but it does not capture all possible effects.

Tables with extinction coefficients and predicted magnitudes of the simulated systems at 10, 20, 50, and 100 au for every band are included in Appendix A (Tables A1–A4). Fig. 9 shows the expected absolute magnitudes of planets with masses 1 (for both viscous and inviscid cases), 2, and $5M_J$ for different distances to the central star, in the *J*, *H*, *K*, *L*, *M*, and *N* bands. The coloured area of each planet represents the uncertainty associated with the column density.

Extinction decreases for planets farther out in the disc due to lower column densities. This behaviour is driven by the surface density profile. Accretion flux is higher at shorter distances, but its effect is minor compared to extinction. Farther out in the disc, the planet magnitude is dominated by the intrinsic flux since the accretion drops with distance. The dispersion of the results is considerable; it cannot be neglected as a source of indeterminacy in our results. Nevertheless, large uncertainties are linked to very high values of the column density, and in such cases, extinction is so strong that the planet would be completely hidden.

At shorter wavelengths (*J*, *H*, and *K* bands), the magnitude of a $1M_J$ planet is completely dominated by extinction: At the farthermost location considered, 100 au, the extinction is 20.4, 13.1, and 8.2 mag in each of these bands. For a $2M_J$ planet, the effect of extinction is lower but still large, e.g. at 100 au, the extinction in these bands is 5.9, 3.8, and 2.4 mag.

The magnitude of a $5M_J$ planet in the simulated disc is barely affected by extinction in any band (the highest extinction coefficient, A_J, ranges from 0.36 to 0.08 between 5.2 and 100 au): Since the

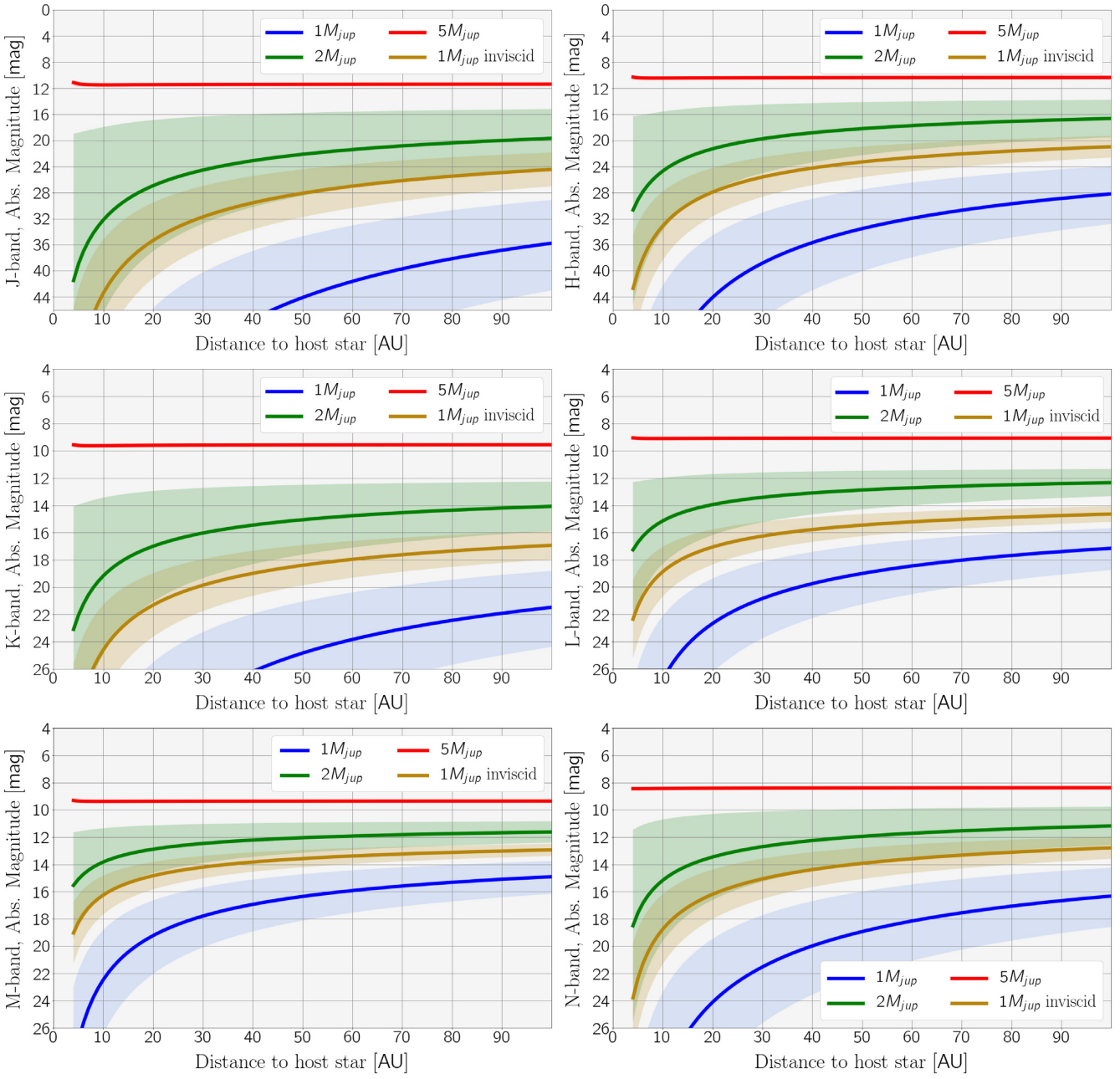

Figure 9. Absolute magnitudes in the *J*, *H*, *K*, *L*, *M*, and *N* bands for the simulated disc with an embedded planet (1, 2, and $5M_J$, or a $1M_J$ planet inviscid case) at different distances to the central star. The results are shown for a *hot-start* model of the formation scenario. The vertical axis for the *J* and *H* bands covers a wider range in order to include all the planets in the same panel.

planet is substantially more massive, it has cleared almost all the material at the gap and its vicinity; thus, both the column density and the extinction coefficients are exceptionally low compared to the other simulated planets.

In the *L* band, the disc material above the least massive planet causes an extinction of 10 mag at 20 au, and is reduced to 4.5 mag at 100 au. A $2M_J$ planet is less affected by extinction, with A_L of 2.9 and 1.3 at those distances. In the *M* band, the extinction coefficients of all the planets considered are the lowest out of all bands considered, nevertheless still considerable except for the $5M_J$ planet. For instance, a $1M_J$ planet at 100 au would be extinct by 3.5 mag. In the *N* band, extinction is increased due to the silicate feature in the opacity of ISM dust: The extinction coefficients are almost two times larger than the coefficients in the *M* band.

Our models can as well be used for different values of the stellar mass. Scaling our results for different $M_\star$ is especially useful when applying our detectability model to real systems, as discussed in the next section. The ratio $M_\star/M_{\rm pl}$ cannot change in order to keep the dynamics of the system valid. The planet mass is rescaled accordingly to keep this ratio constant. Since the planetary models from Spiegel & Burrows (2012) provide data only for planets with 1, 2, 5, or $10M_J$ masses, the planet intrinsic magnitudes were interpolated for the new $M_{\rm pl}$.

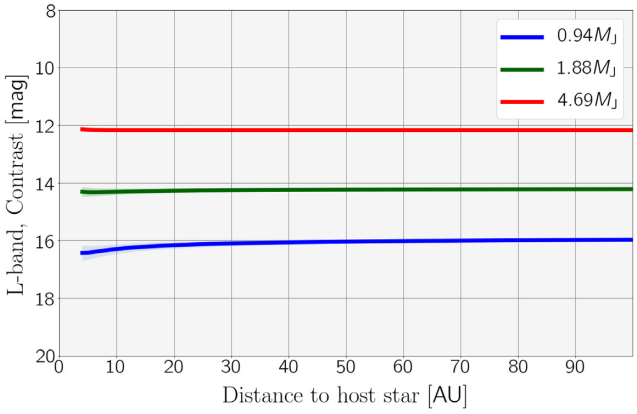

Figure 10. Application of our model to planets with masses 0.94, 1.88, and 4.69M_J embedded in the CQ Tau disc. The coloured lines represent the contrast in the L band of each planet as a function of the distance to the central star placed at different distances along the disc.

4 APPLICATION TO OBSERVED SYSTEMS

Our results can be applied to real systems to study the detectability of embedded planets, as explained in Section 3.2.3. In what follows, we present the results of our model for the Class II discs of CQ Tau, PDS 70, HL Tau, TW Hya, and HD 163296. For the last three systems, our results are combined with contrast limits from previous IR observations (Testi et al. 2015; Ruane et al. 2017; Guidi et al. 2018). The improvement of this revision is the inclusion of the extinction due to the disc material, and the emission from the shocks due to planet accretion.

Additionally, to understand how likely would it be to detect the simulated planets directly with ALMA, we estimated the $1M_J$ planet and CPD fluxes at wavelength 890 μm. The expected planet flux is $\sim 10^{-6}$ mJy, below the ALMA sensitivity limit. For the CPD, simplified to a disc of radius $1R_{\rm Hill}$ centred at the planet and $0.24R_{\rm Hill}$ high (i.e. the region around the planet with a disc-shaped overdensity), we obtain a dust mass of $M_{\rm dust}^{\rm CPD} \approx 0.003\,{\rm M}_\oplus$, which is comparable to the CPD measurements in PDS 70b (Isella et al. 2019). Assuming a constant CPD temperature of 121 K, the continuum emission in ALMA Band 7 would be 0.07 mJy if the emission were assumed optically thin, and 0.23 mJy if optically thick. Thus, the CPD of the simulated disc could be detected by ALMA observations with enough sensitivity.

4.1 CQ Tau

CQ Tau is a young star from the Taurus–Auriga region, spectral type A8 (Trotta et al. 2013) and $M_\star = 1.5\,{\rm M}_\odot$ (Testi et al. 2003). It has an estimated age of ∼5–10 Myr (Chapillon et al. 2008), and a very low disc mass, of the order of 10^{-3}–$10^{-4}\,{\rm M}_\odot$. A fiducial surface density of $\Sigma = 1.6\,{\rm g\,cm^{-2}}$ at 40 au (a factor of × 0.035 of the simulated disc's local surface density) was used for the renormalization to our unperturbed profile, derived from ALMA observations (Ubeira Gabellini et al. 2019).

We applied our models to investigate the effects of disc extinction on potential planets embedded in the disc. Due to the rescaling with the stellar mass, the contrast curves are derived for planets with masses 0.94, 1.88, and 4.69M_J. A distance of 163.1 pc (Gaia Collaboration et al. 2018) was used for the predicted contrast. Fig. 10 shows the contrast of the planets in the L band as a function of distance to the central star; the planet contrast is shown relative to the stellar value. The coloured area for each planet represents the associated dispersion. The results in the J, H, and K bands are included in Appendix B.

At a fixed distance, the more massive the planet, the less affected by extinction, since the planet is more effective at clearing the gap. Due to the very low surface density inferred from the ALMA observations, extinction in the L band is relevant only for the lightest planets. At 20 au, a $0.94M_J$ planet would have a contrast of 16.16 mag and extinction $A_L = 0.34$ mag ($A_V = 5.47$ mag). The contrast of a $1.88M_J$ planet is 14.27 mag with an extinction of only 0.10 mag ($A_V = 1.60$ mag). The most massive planet ($4.69M_J$) is barely affected by extinction, and its contrast is equivalent to the case of a completely depleted disc, 12.17 mag.

4.2 PDS 70

PDS 70 is a member of the Upper Centaurus–Lupus subgroup (at ∼113 pc, Gaia Collaboration et al. 2018), with a central star of 5.4 Myr and mass 0.76 $\rm M_\odot$ (Müller et al. 2018). It is surrounded by a transition disc with an estimated total disc mass of $1 \times 10^{-3}\,{\rm M}_\odot$. A first companion (PDS 70b) was found combining observations with VLT/SPHERE, VLT/NaCo, and Gemini/NICI at various epochs, detected as a point source in the H, K, and L bands at a projected averaged separation of 194.7 mas (Keppler et al. 2018). In the J band, PDS 70b could only be marginally detected when collapsing the J- and H-band channels. Due to the high uncertainties, J-band magnitude was not given. Atmospheric modelling of the planet was used to constrain its properties (Müller et al. 2018), with an estimated mass range from 2 to $17M_J$.

Recent Hα line observations using VLT/MUSE confirmed a 8σ detection from a second companion (PDS 70c) at 240 mas (Haffert et al. 2019). Dust continuum emission (likely from its CPD) has been also observed (Isella et al. 2019). This second source is very close to an extended disc feature; consequently, its photometry should be done with caution. In Mesa et al. (2019), the planetary nature of this companion has been confirmed, and absolute magnitudes in the J, H, and K bands could be inferred for two SPHERE epochs. The spectrum in the J band is very faint, and indistinguishable from the adjacent disc feature; thus, the J-band magnitude should be regarded as an upper limit. The NaCo L-band map detected emission is partly covered by the disc; therefore, its L-band magnitude should also be taken as an upper limit. Using various atmospheric models, Mesa et al. (2019) constrained the mass of PDS 70c to be between 1.9 and $4.4M_J$.

Our models were rescaled using a fiducial surface density of $\Sigma = 12.5\,{\rm g\,cm^{-2}}$ at 1 au (taking the unperturbed surface density model with depletion factor $\delta_{\rm disc} = 1$ and a gas-to-dust ratio of 100, from Keppler et al. 2018). This corresponds to a surface density scale factor of × 0.043 with respect to the simulated disc. From the rescaling, we obtained contrast curves of planets embedded in the PDS 70 disc with masses 0.48, 0.95, and $2.38M_J$ (Fig. 11). The results show the effect of a disc with a very low surface density: Extinction has an incidence in the J and H bands for 0.95 and $0.48M_J$ planets located within $\lesssim$40 au. In the L band, extinction has only a minor effect on the lightest planet model at distances below 20 au. From the assumed surface density profile, none of the planetary companions would be affected by extinction due to material from the protoplanetary disc in the IR bands.

The observed contrast of the primary companion in the three bands is considerably higher than the value for the most massive planet of our models, thus setting a mass lower limit of $2.38M_J$ for PDS 70b. The second companion lies on top of the $2.38M_J$ model in

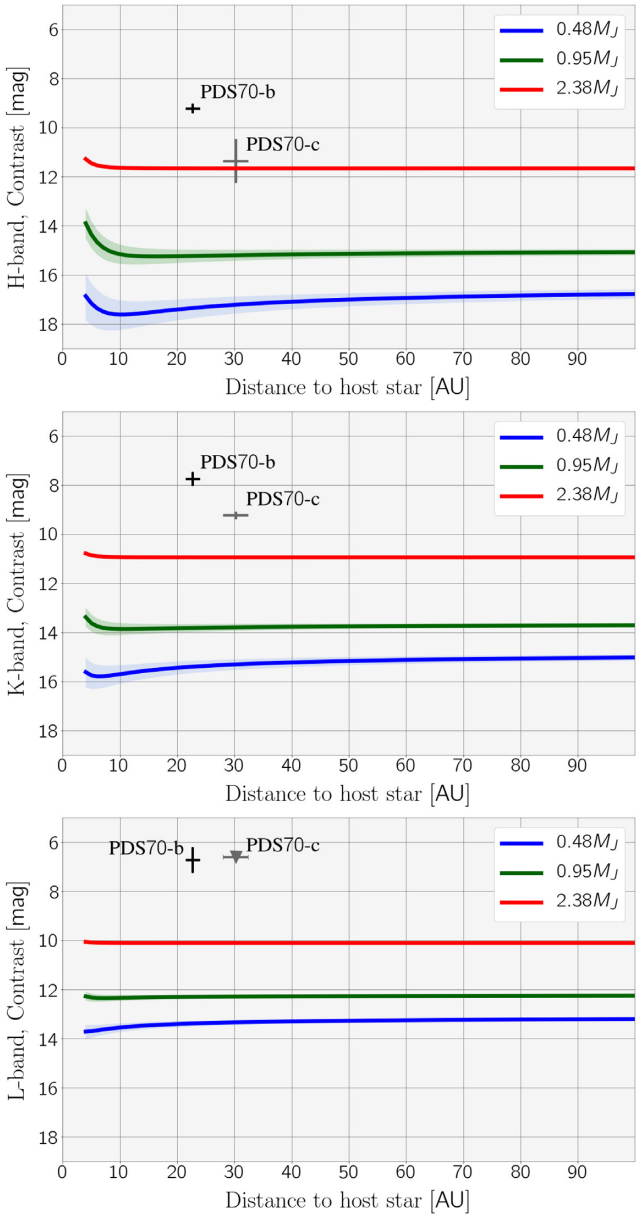

Figure 11. Application of our model to planets with masses 0.48, 0.95, and 2.38M_J embedded in the PDS 70 disc. The contrast curves shown for the H, K, and L bands were obtained considering stellar magnitudes of $H = 8.8$ mag, $K = 8.5$ mag, and $L = 7.9$ mag (Cutri et al. 2003; Cutri & et al. 2014). The two planetary companions (Keppler et al. 2018; Haffert et al. 2019; Mesa et al. 2019) are shown as black and grey crosses, with the corresponding uncertainties.

the H band, and above it in the K band. The redness of this source can explain the difference in the band contrast. This reddening might be due to the material from its own CPD or from the contiguous disc feature. Our models are in agreement with the previous mass ranges estimated for the two companions; further observations and modelling of the disc and their atmospheres are needed to better constrain their masses.

The estimated accretion rates of the companions are of the order of $\sim 10^{-11}$ $M_\odot\,yr^{-1}$ (Haffert et al. 2019); thus, the radiation from accretion shocks near both planets is negligible. From our results, accretion flux would have an incidence only in the modelled IR

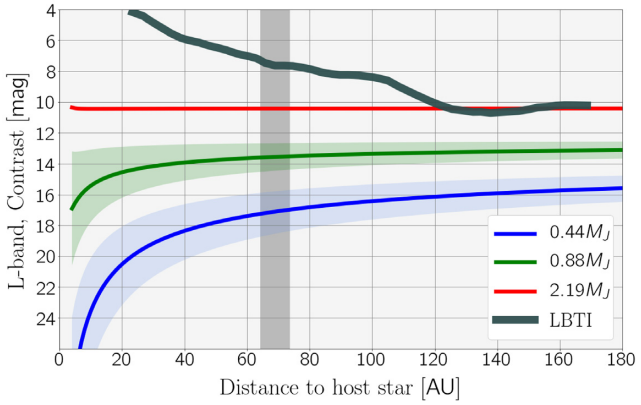

Figure 12. Contrast curves in the L band for planets embedded in HL Tau, including the 5σ detection limit of the observation from Testi et al. (2015). The observations were performed using LBTI/LMIRcam. The contrast curves are for planet masses of 0.44, 0.88, and 2.19M_J. The considered apparent magnitude of the central star was $L = 6.23$ mag (Testi et al. 2015). The coloured regions account for the uncertainty in the planet contrast. The grey vertical area is delimited by the D5 and D6 rings detected in dust continuum (ALMA Partnership et al. 2015).

planet fluxes at distances $\sim$5 au, since accretion rates are expected to be higher due to the scaling. This can be appreciated in the contrast curve of the three planet models in the H band: Planets' contrasts decrease at these distances. The effect of the accretion shock's radiation becomes negligible at $\gtrsim$10 au.

4.3 HL Tau

HL Tau is one of the most extensively studied protoplanetary discs, with several rings and gaps detected in the dust continuum (ALMA Partnership et al. 2015). It is a young stellar object of $\leq$1 Myr at around 140 pc to us (Kenyon, Gómez & Whitney 2008), with an estimated stellar mass of $\sim$0.7 $M_\odot$ (Kenyon & Hartmann 1995; Close et al. 1997). Observations were carried out using the LBTI L/M IR Camera (LMIRcam, Skrutskie et al. 2010; Leisenring et al. 2012), using only one of the two primary mirrors of the LBT telescope. No point sources were detected. For the normalization of the surface density, we took the inferred gas surface density from CARMA observations (Kwon, Looney & Mundy 2011; Kwon et al. 2015) at a fiducial distance of 40 au, $\Sigma = 34$ g cm^{-2} (a factor of $\times$ 0.74 compared to the simulated disc).

In Fig. 12, we show the contrast limit of the LBTI observation in the L band as a function of the angular separation to the central star, together with the derived contrast of the rescaled models for planets with masses 0.44, 0.88, and 2.19M_J. In Appendix B, contrast curves in the J, H, and K bands are included for completeness. In the L band, a high extinction is predicted for 0.44 and 0.88M_J planets along the entire disc, especially at distances $\lesssim$ 60 au; at that distance, A_L values are 4.27 mag ($A_V = 68.29$ mag) and 1.25 mag ($A_V = 19.98$ mag) for these planets, respectively. For planets outer in the disc, the extinction contribution is smaller but still significant: 3.02 mag ($A_V = 48.29$ mag) for 0.44M_J and 0.88 mag ($A_V = 14.13$ mag) for 0.88M_J at 120 au. These planets are not massive enough to clear the gap efficiently. On the other hand, for the most massive planet (2.19M_J), extinction is negligible at any distance.

Six gaps were observed in the ALMA continuum observation; following the example in Testi et al. (2015), within the gap delimited by D5 and D6 rings (marked as a grey vertical line),

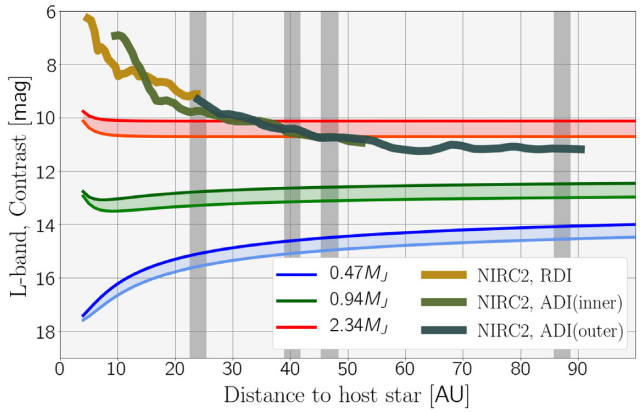

Figure 13. Contrast curves in the *L* band for planets embedded in TW Hya, including 95 per cent significance detection limits of Keck/NIR2 observations (Ruane et al. 2017). The contrast limits are shown for ADI and RDI. The contrast curves shown are for planet masses of 0.47, 0.94, and 2.34M_J. The apparent magnitude of the central star is $L = 7.01$ mag, taken from the *W1* band in the *WISE* catalogue (Wright et al. 2010). The coloured regions for each planet model are delimited by the estimated ages (7–10 Myr, Ruane et al. 2017). The grey vertical lines account for the gaps observed in Andrews et al. (2016) and van Boekel et al. (2017).

the contrast limit of the instrument does not allow us to constrain the mass of the companion, which could be responsible for the gap. Nevertheless, from the inferred contrast curves, extinction would have an incidence in a hypothetical point-source detection only for planet masses $\lesssim 0.88 M_J$.

4.4 TW Hya

Observations using the Keck/NIRC2 vortex coronagraph were performed by Ruane et al. (2017) searching for point sources in the TW Hya disc. This system is the closest known protoplanetary disc to us (60.2 au, Gaia Collaboration et al. 2018), with a central star of 0.7–0.8 $M_\odot$ (Andrews et al. 2012; Herczeg & Hillenbrand 2014), relatively old (7–10 Myr, Ruane et al. 2017), and with an estimated total disc mass of 0.05 $M_\odot$ (Bergin et al. 2013). The surface gas density has been modelled from ALMA line-emission observations (Kama et al. 2016; Trapman et al. 2017). From their unperturbed models, we used a fiducial surface density of 10.9 g cm^{-2} at 40 au for the rescaling (a surface density factor of $\times$ 0.24 of the simulated disc). The instrument allows for IR high-contrast imaging in the *L* band, using angular differential imaging (ADI) and reference star differential imaging (RDI). In Fig. 13, the detection limits for ADI and RDI are shown together with the expected contrast of planets with masses 0.47, 0.94, and 2.34M_J. In this observation, RDI allows for detections of point sources at distances as low as ~5 au. At this distance, the accretion flux overcomes the intrinsic flux for a planet of mass $\gtrsim 2.34 M_J$; thus, the contrast decreases compared to the non-accreting case. The contrast curves of these planets in the *J*, *H*, and *K* bands are shown in Appendix B.

Different observations of TW Hya confirmed several gaps in the disc. Andrews et al. (2016) detected three dark annuli at distances 24, 41, and 47 au to the host star (distances corrected with the newest *Gaia* parallax). An unresolved gap in the inner disc was also seen from 870 μm continuum emission using ALMA. Scattered light using SPHERE detected three gaps in the polarized intensity distribution, at $\lesssim$7, 23, and 88 au. In the figure, we show the gaps in the outer disc (at ~23, 40, 46, and 87 au). No point sources were detected in the Keck/NIRC2 observations. Ruane et al. (2017) set mass upper limits for planets located at these gaps (1.6–2.3, 1.1–1.6, 1.1–1.5, and 1.0–1.2M_J from inner to outer distances). Analogously, we can infer upper limits of the planets interpolating our results, since the contrast curves lie between our models. Using the models for 7-Myr planets, the mass upper limits for these gaps would be 2.5, 2.1, 2.0, and 1.7M_J, respectively. Considering an age of 10 Myr, the upper limits are marginally higher: 2.8, 2.4, 2.3, and 2.1M_J, respectively. Taking into account the extinction due to the disc above the planet increases the estimated upper limits compared to the previous work, which did not consider this effect. This indicates the importance of extinction when looking for protoplanets with direct imaging methods.

4.5 HD 163296

In Guidi et al. (2018), the HD 163296 disc was studied in the *L* band using the same instrument (Keck/NIRC2 vortex coronagraph). The scattered polarized emission in the *J* band was also studied with the Gemini Planet Imager in Monnier et al. (2017), detecting a ring with an offset that can be explained by an inclined flared disc. This system has a central star of 2.3 $M_\odot$ (Natta et al. 2004) and estimated age of ~5 Myr (Montesinos et al. 2009). Observations in the dust continuum using ALMA (Isella et al. 2016) confirmed the existence of three gaps at distances of ~50, ~81, and ~136 au (corrected with the new *Gaia* distance of 101.5 pc). Kinematical analysis of gas observations suggested the presence of two planets at the second and third gaps (Teague et al. 2018). In Pinte et al. (2018), HD models showed that a third planet is expected farther out. The estimated masses of the three potential planets are 1M_J (at 83 au), 1.3M_J (at 127 au), and $\approx$2M_J (at $\approx$260 au). The new DSHARP/ALMA observations confirmed an additional gap at ~10 au (Isella et al. 2018); assuming that this gap is caused by a planet, Zhang et al. (2018) estimated a planet mass between 0.2 and 1.5M_J from 2D HD simulations.

The *L*-band high-contrast imaging (Guidi et al. 2018) detected a point-like source at a distance of 67.7 au with significance 4.7σ. None of the observations in the *L* or *J* band found any point sources at the gaps observed in the continuum. Our models allow us to set upper limits for planets at the location of the gaps. We used a fiducial surface density of $\Sigma = 82.8$ g cm^{-2} at 40 au (from Isella et al. 2016), corresponding to a factor of $\times$ 1.8 of the simulated disc, to obtain contrast curves for 1.44, 2.88, and 7.19 M_J (*L* band in Fig. 14, and *J*, *H*, and *K* bands in Fig. B4 in Appendix B). The innermost gap in Fig. 14 is within the masked region in the Keck/NIR2 observations; thus, a mass upper limit cannot be inferred. At the second gap, the model for our most massive planet lies slightly below the detection limit of the observation. A rough extrapolation would yield an upper limit of 7.6M_J, slightly below the range provided by Guidi et al. (2018) (8–15M_J in that work). For the third and fourth gaps, we obtain upper limits of 6.7 and 5.5M_J from interpolating our models. These values are slightly higher than the upper limits inferred in Guidi et al. (2018) (4.5–6.5 and 2.5–4M_J, respectively). Taking into account extinction on the contrast of the planets increases the inferred upper limits of the non-detected planets. In every gap, extinction does have an important effect for planets with masses lower than the inferred upper limits. Compared to the estimates of Teague et al. (2018) and Pinte et al. (2018) from indirect analysis, our inferred upper limits are significantly higher; consequently, a direct detection of these companions would be possible only by improving the detection limit to a much higher contrast.

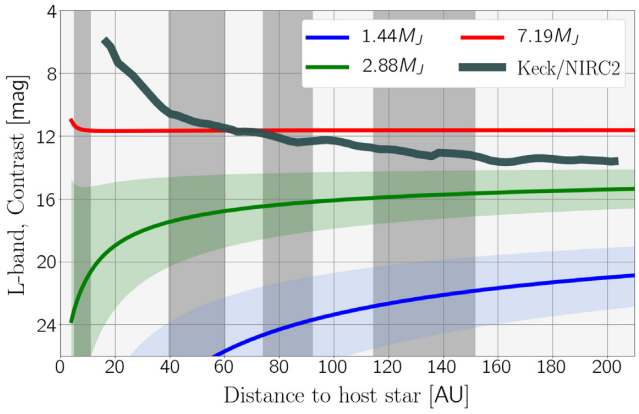

Figure 14. Contrast curves in the L band for planets embedded in HD 163296, including the 5σ detection limits of the observation from Guidi et al. (2018). The observations were performed using Keck/NIRC2. The contrasts of planets with masses 1.44, 2.88, and 7.19M_J are shown. The apparent magnitude of the central star is $L = 3.7$ mag, inferred from the *W1* band in the *WISE* catalogue (Wright et al. 2010). The grey vertical lines account for the gaps observed in Isella et al. (2016, 2018).

5 CONCLUSIONS

In this work, we studied the effect of extinction on direct imaging of young planets embedded in protoplanetary discs. A set of HD simulations were performed to reproduce the planet–disc interaction at high resolution for several planet masses. Column densities and extinction coefficients were derived in order to model the planet predicted magnitudes in the J, H, K, L, M, and N bands. Exploiting properties of locally isothermal discs, we applied the models to planets embedded in CQ Tau, PDS 70, and HL Tau protoplanetary discs, and inferred upper limits for planets at the gaps observed in TW Hya and HD 163296. The most important results of this work are as follows:

(i) For the simulated planets at 5.2 au, the $5M_J$ planet clears its surrounding material very effectively. The resulting column density is extremely low, and, as a consequence, extinction is not significant in any band. The 1 and $2M_J$ planets are completely hidden by the disc at $\lesssim 2$ μm wavelengths (with respective extinction coefficients of >30 and >15 mag), while at wavelengths between 5 and 8 μm, their corresponding coefficients are reduced, below 15 and 4 mag. In the N band, extinction is higher compared to the L and N bands due to the silicate feature in the assumed ISM dust opacities.

(ii) Jupiter-like planets embedded in discs with very low unperturbed surface densities (of the order of $\lesssim 1$ g cm^{-2}) have very low extinction coefficients in the IR at any distance considered. In CQ Tau, only planets with mass $\lesssim 2M_J$ are affected by extinction in the J and H bands at distances $\lesssim 20$ au. In PDS 70, extinction has an incidence only for the least massive planet model at distances $<$ 50 au, more significant at shorter wavelengths.

(iii) In more dense discs like HL Tau and HD 163296, a direct detection of companions is unlikely in the J, H, K, and N bands due to the extinction effects. Only the most massive planet from our models would be detectable, since the extinction is negligible.

(iv) We inferred upper limits of the gaps in TW Hya and HD 163296, slightly higher than previous work due to the effect of extinction. This points out the importance of extinction from the disc material in high-contrast imaging of protoplanetary discs.

(v) Radiation from accretion shocks on to the planet has been considered in our models. It can have an important effect on the total planet emission for accretion rates of the order of $\sim 10^{-8}$ $M_\odot$ yr^{-1}; these high rates occur at distances $\lesssim 10$ au in our models.

The scarcity of detections so far might suggest different scenarios: Giant planet formation farther out in the disc is rare, or perhaps planets formed at these early stages are still not massive enough ($\lesssim 2M_J$) to be detected with the current instrumentation.

ACKNOWLEDGEMENTS

This work was partly supported by the Italian Ministero dell' Istruzione, Università e Ricerca, through the grant Progetti Premiali 2012 – iALMA (CUP C52I13000140001), by the Deutsche Forschungsgemeinschaft (DFG, German Research Foundation) – Ref no. FOR 2634/1 TE 1024/1-1, and by the DFG cluster of excellence Origin and Structure of the Universe (www.universe-cluster.de). This work is part of the research programme VENI with project number 016.Veni.192.233, which is (partly) financed by the Dutch Research Council (NWO). The simulations were partly run on the computing facilities of the Computational Center for Particle and Astrophysics (C2PAP) of the Excellence Cluster Universe. BE acknowledges funding by the Deutsche Forschungsgemeinschaft (DFG, German Research Foundation) under Germany's Excellence Strategy – EXC-2094–390783311. GP and BE acknowledge support from the DFG Research Unit 'Transition Disks' (FOR 2634/1, ER 685/8-1).

REFERENCES

ALMA Partnership et al., 2015, ApJ, 808, L3
Andrews S. M., 2015, PASP, 127, 961
Andrews S. M. et al., 2012, ApJ, 744, 162
Andrews S. M. et al., 2016, ApJ, 820, L40
Andrews S. M. et al., 2018, ApJ, 869, L41
Ansdell M., Williams J. P., Manara C. F., Miotello A., Facchini S., van der Marel N., Testi L., van Dishoeck E. F., 2017, AJ, 153, 240
Beccari G. et al., 2010, ApJ, 720, 1108
Bergin E. A. et al., 2013, Nature, 493, 644
Brown J. M., Blake G. A., Qi C., Dullemond C. P., Wilner D. J., 2008, ApJ, 675, L109
Bryden G., Chen X., Lin D. N. C., Nelson R. P., Papaloizou J. C. B., 1999, ApJ, 514, 344
Cardelli J. A., Clayton G. C., Mathis J. S., 1989, ApJ, 345, 245
Chapillon E., Guilloteau S., Dutrey A., Piétu V., 2008, A&A, 488, 565
Chiar J. E., Tielens A. G. G. M., 2006, ApJ, 637, 774
Close L. M., Roddier F., J. Northcott M., Roddier C., Elon Graves J., 1997, ApJ, 478, 766
Cutri R. M. et al., 2003, VizieR Online Data Catalog, 2246
Cutri R. M. et al., 2014, VizieR Online Data Catalog, 2328
D'Angelo G., Kley W., Henning T., 2003, ApJ, 586, 540
Dipierro G., Laibe G., 2017, MNRAS, 469, 1932
Dong R., Fung J., 2017, ApJ, 835, 146
Dong R., Zhu Z., Whitney B., 2015a, ApJ, 809, 93
Dong R., Zhu Z., Rafikov R. R., Stone J. M., 2015b, ApJ, 809, L5
Duffell P. C., 2015, ApJ, 806, 182
Dürmann C., Kley W., 2015, A&A, 574, A52
Ercolano B., Pascucci I., 2017, R. Soc. Open Sci., 4, 170114
Frank J., King A. R., Raine D. J., 1985, Accretion Power in Astrophysics. Cambridge University Press, The Pitt Building, Trumpington Street, Cambridge CB2 1RP.
Fung J., Dong R., 2015, ApJ, 815, L21
Gaia Collaboration et al., 2018, A&A, 616, A1
Guidi G. et al., 2018, MNRAS, 479, 1505
Güver T., Özel F., 2009, MNRAS, 400, 2050

Haffert S. Y., Bohn A. J., de Boer J., Snellen I. A. G., Brinchmann J., Girard J. H., Keller C. U., Bacon R., 2019, Nature Astron., 3, 749
Hartmann L., 1998, Accretion Processes in Star Formation. Cambridge Univ. Press, Cambridge
Hartmann L., Herczeg G., Calvet N., 2016, ARA&A, 54, 135
Hayashi C., 1981, Prog. Theor. Phys. Suppl., 70, 35
Herczeg G. J., Hillenbrand L. A., 2014, ApJ, 786, 97
Hernández J., Hartmann L., Calvet N., Jeffries R. D., Gutermuth R., Muzerolle J., Stauffer J., 2008, ApJ, 686, 1195
Isella A. et al., 2016, Phys. Rev. Lett., 117, 251101
Isella A. et al., 2018, ApJ, 869, L49
Isella A., Benisty M., Teague R., Bae J., Keppler M., Facchini S., Pérez L., 2019, ApJ, 879, L25
Jang-Condell H., 2009, ApJ, 700, 820
Jang-Condell H., 2017, ApJ, 835, 12
Jang-Condell H., Turner N. J., 2013, ApJ, 772, 34
Juhász A., Rosotti G. P., 2018, MNRAS, 474, L32
Juhász A., Benisty M., Pohl A., Dullemond C. P., Dominik C., Paardekooper S. J., 2015, MNRAS, 451, 1147
Kama M. et al., 2016, A&A, 592, A83
Kenyon S. J., Hartmann L., 1995, ApJS, 101, 117
Kenyon S. J., Gómez M., Whitney B. A., 2008, Handbook of Star Forming Regions, I: The Northern Sky, Astronomical Society of the Pacific, 390 Ashton Avenue, San Francisco, California, 94112-1722, USA. p. 405
Keppler M. et al., 2018, A&A, 617, A44
Klahr H., Kley W., 2006, A&A, 445, 747
Kley W., 1999, MNRAS, 303, 696
Kwon W., Looney L. W., Mundy L. G., 2011, ApJ, 741, 3
Kwon W., Looney L. W., Mundy L. G., Welch W. J., 2015, ApJ, 808, 102
Leisenring J. M. et al., 2012, in McLean I. S., Ramsay S. K., Takami H., eds, Proc. SPIE Conf. Ser. Vol. 8446, Ground-Based and Airborne Instrumentation for Astronomy IV. SPIE, Bellingham. p. 84464F
Manara C. F., Morbidelli A., Guillot T., 2018, A&A, 618, L3
Mendigutía I., Calvet N., Montesinos B., Mora A., Muzerolle J., Eiroa C., Oudmaijer R. D., Merín B., 2011, A&A, 535, A99
Meru F., Rosotti G. P., Booth R. A., Nazari P., Clarke C. J., 2019, MNRAS, 482, 3678
Mesa D. et al., 2019, A&A, 632, A25
Mignone A., Tzeferacos P., Zanni C., Tesileanu O., Matsakos T., Bodo G., 2010, PLUTO: A Code for Flows in Multiple Spatial Dimensions, Astrophysics Source Code Library. record ascl:1010.045
Mignone A., Zanni C., Tzeferacos P., van Straalen B., Colella P., Bodo G., 2012, ApJS, 198, 7
Miotello A. et al., 2017, A&A, 599, A113
Monnier J. D. et al., 2017, ApJ, 838, 20
Montesinos B., Eiroa C., Mora A., Merín B., 2009, A&A, 495, 901
Müller A. et al., 2018, A&A, 617, L2
Natta A., Testi L., Neri R., Shepherd D. S., Wilner D. J., 2004, A&A, 416, 179
Nazari P., Booth R. A., Clarke C. J., Rosotti G. P., Tazzari M., Juhasz A., Meru F., 2019, MNRAS, 485, 5914
Nelson R. P., Gressel O., Umurhan O. M., 2013, MNRAS, 435, 2610
Ormel C. W., Paszun D., Dominik C., Tielens A. G. G. M., 2009, A&A, 502, 845
Ormel C. W., Min M., Tielens A. G. G. M., Dominik C., Paszun D., 2011, A&A, 532, A43
Ormel C. W., Kuiper R., Shi J.-M., 2015a, MNRAS, 446, 1026
Ormel C. W., Shi J.-M., Kuiper R., 2015b, MNRAS, 447, 3512
Paardekooper S.-J., 2017, MNRAS, 469, 4306
Paardekooper S. J., Mellema G., 2006, A&A, 453, 1129
Piétu V., Dutrey A., Guilloteau S., Chapillon E., Pety J., 2006, A&A, 460, L43
Pinte C. et al., 2018, ApJ, 860, L13
Pollack J. B., Hollenbach D., Beckwith S., Simonelli D. P., Roush T., Fong W., 1994, ApJ, 421, 615
Quanz S. P., Amara A., Meyer M. R., Girard J. H., Kenworthy M. A., Kasper M., 2015, ApJ, 807, 64
Rameau J., Chauvin G., Lagrange A.-M., Maire A.-L., Boccaletti A., Bonnefoy M., 2015, A&A, 581, A80
Reggiani M. et al., 2014, ApJ, 792, L23
Reggiani M. et al., 2018, A&A, 611, A74
Rice W. K. M., Armitage P. J., Wood K., Lodato G., 2006, MNRAS, 373, 1619
Rosotti G. P., Juhasz A., Booth R. A., Clarke C. J., 2016, MNRAS, 459, 2790
Ruane G. et al., 2017, AJ, 154, 73
Scicluna P., Rosotti G., Dale J. E., Testi L., 2014, A&A, 566, L3
Shakura N. I., Sunyaev R. A., 1973, A&A, 24, 337
Skrutskie M. F. et al., 2010, in McLean I. S., Ramsay S. K., Takami H., eds, Proc. SPIE Conf. Ser. Vol. 7735, Ground-Based and Airborne Instrumentation for Astronomy III. SPIE, Bellingham. p. 77353H.
Spiegel D. S., Burrows A., 2012, ApJ, 745, 174
Szulágyi J., Morbidelli A., Crida A., Masset F., 2014, ApJ, 782, 65
Szulágyi J., Masset F., Lega E., Crida A., Morbidelli A., Guillot T., 2016, MNRAS, 460, 2853
Tanigawa T., Watanabe S.-i., 2002, ApJ, 580, 506
Tazzari M. et al., 2016, A&A, 588, A53
Tazzari M. et al., 2017, A&A, 606, A88
Teague R., Bae J., Bergin E. A., Birnstiel T., Foreman-Mackey D., 2018, ApJ, 860, L12
Testi L., Natta A., Shepherd D. S., Wilner D. J., 2003, A&A, 403, 323
Testi L. et al., 2015, ApJ, 812, L38
Trapman L., Miotello A., Kama M., van Dishoeck E. F., Bruderer S., 2017, A&A, 605, A69
Trotta F., Testi L., Natta A., Isella A., Ricci L., 2013, A&A, 558, A64
Ubeira Gabellini M. G. et al., 2019, MNRAS, 486, 4638
van Boekel R. et al., 2017, ApJ, 837, 132
Wolf S., D'Angelo G., 2005, ApJ, 619, 1114
Wright E. L. et al., 2010, AJ, 140, 1868
Zhang S. et al., 2018, ApJ, 869, L47
Zhu Z., 2015, ApJ, 799, 16

APPENDIX A: MAGNITUDES FOR PLANETS AT 10, 20, 50, AND 100 AU

The predicted magnitudes of the modelled planets at various distances to the central star are included in Tables A1–A4 for completeness.

Table A1. Expected magnitudes for planets at 10 au to the host star, with masses $1M_J$ – viscous and inviscid scenarios – $2M_J$, and $5M_J$. Mag_{pl} is the total magnitude of the planet, including accretion flux; A_{band} is the extinction coefficient in each band; and $Mag_{expected}$ is the predicted magnitude of the planet considering extinction due to disc material.

		Hot-start planet						*Cold-start* planet					
		J	*H*	*K*	*L*	*M*	*N*	*J*	*H*	*K*	*L*	*M*	*N*
	Mag_{pl}	15.13	14.95	13.31	12.65	11.40	10.02	15.92	16.02	15.95	14.94	12.97	12.01
$1M_J$	A_{band}	64.58	41.30	25.99	14.11	11.05	19.91	64.58	41.30	25.99	14.11	11.05	19.91
	$Mag_{expected}$	79.70	56.25	39.30	26.76	22.45	29.93	80.49	57.32	41.94	29.05	24.03	31.91
	Mag_{pl}	13.55	12.76	11.66	11.01	10.59	9.34	14.93	15.01	15.00	14.12	12.64	11.82
$2M_J$	A_{band}	18.62	11.91	7.49	4.13	3.23	5.82	18.62	11.91	7.49	4.13	3.23	5.82
	$Mag_{expected}$	32.17	24.67	19.16	15.14	13.82	15.16	33.55	26.92	22.50	18.25	15.88	17.64
	Mag_{pl}	11.25	10.28	9.52	9.04	9.33	8.35	14.80	14.84	14.89	13.52	12.39	11.76
$5M_J$	A_{band}	0.26	0.16	0.10	0.06	0.04	0.08	0.26	0.16	0.10	0.06	0.04	0.08
	$Mag_{expected}$	11.51	10.44	9.62	9.10	9.38	8.43	15.05	15.00	14.99	13.58	12.44	11.84
	Mag_{pl}	15.53	15.25	13.36	12.68	11.41	10.03	17.51	17.69	17.27	15.33	13.02	12.02
$1M_{inviscid}$	A_{band}	27.86	17.82	11.21	6.18	4.84	8.71	27.86	17.82	11.21	6.18	4.84	8.71
	$Mag_{expected}$	43.39	33.07	24.58	18.86	16.25	18.74	45.37	35.51	28.49	21.51	17.86	20.74

Table A2. Absolute magnitudes for planets at 20 au to the host star, with masses $1M_J$ – viscous and inviscid scenarios – $2M_J$, and $5M_J$. Mag_{pl} is the total magnitude of the planet, including accretion flux; A_{band} is the extinction coefficient in each band; and $Mag_{expected}$ is the predicted magnitude of the planet considering extinction due to disc material.

		Hot-start planet						*Cold-start* planet					
		J	*H*	*K*	*L*	*M*	*N*	*J*	*H*	*K*	*L*	*M*	*N*
	Mag_{pl}	15.55	15.27	13.37	12.68	11.41	10.03	17.77	17.98	17.45	15.36	13.02	12.02
$1M_J$	A_{band}	45.66	29.20	18.38	9.98	7.82	14.08	45.66	29.20	18.38	9.98	7.82	14.08
	$Mag_{expected}$	61.22	44.47	31.74	22.66	19.22	24.10	63.43	47.18	35.83	25.34	20.84	26.10
	Mag_{pl}	13.76	12.85	11.69	11.03	10.60	9.34	16.86	16.91	16.70	14.64	12.74	11.85
$2M_J$	A_{band}	13.17	8.42	5.30	2.92	2.29	4.12	13.17	8.42	5.30	2.92	2.29	4.12
	$Mag_{expected}$	26.93	21.28	16.99	13.95	12.89	13.46	30.03	25.33	22.00	17.56	15.02	15.97
	Mag_{pl}	11.28	10.29	9.52	9.05	9.34	8.35	16.61	16.50	16.55	14.16	12.55	11.83
$5M_J$	A_{band}	0.18	0.12	0.07	0.04	0.03	0.06	0.18	0.12	0.07	0.04	0.03	0.06
	$Mag_{expected}$	11.46	10.40	9.59	9.09	9.37	8.41	16.79	16.61	16.62	14.20	12.58	11.89
	Mag_{pl}	15.62	15.32	13.38	12.69	11.41	10.03	18.59	18.94	17.92	15.43	13.03	12.03
$1M_{inviscid}$	A_{band}	19.70	12.60	7.93	4.37	3.42	6.16	19.70	12.60	7.93	4.37	3.42	6.16
	$Mag_{expected}$	35.32	27.92	21.30	17.06	14.83	16.19	38.29	31.54	25.84	19.79	16.45	18.19

Table A3. Expected magnitudes for planets at 50 au to the host star, with masses $1M_J$ – viscous and inviscid scenarios – $2M_J$, and $5M_J$. Mag_{pl} is the total magnitude of the planet, including accretion flux; A_{band} is the extinction coefficient in each band; and $Mag_{expected}$ is the predicted magnitude of the planet considering extinction due to disc material.

		Hot-start planet						*Cold-start* planet					
		J	*H*	*K*	*L*	*M*	*N*	*J*	*H*	*K*	*L*	*M*	*N*
	Mag_{pl}	15.63	15.32	13.38	12.69	11.41	10.03	18.77	19.18	18.00	15.43	13.03	12.03
$1M_J$	A_{band}	28.88	18.47	11.62	6.31	4.94	8.90	28.88	18.47	11.62	6.31	4.94	8.90
	$Mag_{expected}$	44.51	33.79	25.00	19.00	16.35	18.93	47.65	37.65	29.62	21.75	17.97	20.93
	Mag_{pl}	13.80	12.87	11.70	11.03	10.60	9.34	18.03	18.00	17.46	14.73	12.75	11.86
$2M_J$	A_{band}	8.33	5.33	3.35	1.85	1.45	2.60	8.33	5.33	3.35	1.85	1.45	2.60
	$Mag_{expected}$	22.12	18.19	15.05	12.88	12.05	11.94	26.35	23.33	20.81	16.58	14.20	14.46
	Mag_{pl}	11.28	10.29	9.52	9.05	9.34	8.35	17.53	17.21	17.27	14.28	12.57	11.84
$5M_J$	A_{band}	0.11	0.07	0.05	0.03	0.02	0.04	0.11	0.07	0.05	0.03	0.02	0.04
	$Mag_{expected}$	11.39	10.36	9.57	9.08	9.36	8.39	17.65	17.28	17.31	14.31	12.59	11.88
	Mag_{pl}	15.64	15.33	13.38	12.69	11.41	10.03	18.87	19.32	18.04	15.44	13.03	12.03
$1M_{inviscid}$	A_{band}	12.46	7.97	5.01	2.76	2.16	3.90	12.46	7.97	5.01	2.76	2.16	3.90
	$Mag_{expected}$	28.10	23.30	18.39	15.45	13.57	13.93	31.32	27.29	23.05	18.20	15.19	15.93

Table A4. Expected magnitudes for planets at 100 au to the host star, with masses $1M_J$ – viscous and inviscid scenarios – $2M_J$, and $5M_J$. Mag_{pl} is the total magnitude of the planet, including accretion flux; A_{band} is the extinction coefficient in each band; and $Mag_{expected}$ is the predicted magnitude of the planet considering extinction due to disc material.

		Hot-start planet						*Cold-start* planet					
		J	*H*	*K*	*L*	*M*	*N*	*J*	*H*	*K*	*L*	*M*	*N*
	Mag_{pl}	15.63	15.33	13.38	12.69	11.41	10.03	18.87	19.33	18.04	15.44	13.03	12.03
$1M_J$	A_{band}	20.42	13.06	8.22	4.46	3.50	6.30	20.42	13.06	8.22	4.46	3.50	6.30
	$Mag_{expected}$	36.06	28.39	21.60	17.15	14.90	16.32	39.29	32.39	26.26	19.90	16.52	18.32
	Mag_{pl}	13.80	12.87	11.70	11.03	10.60	9.34	18.16	18.12	17.53	14.74	12.75	11.86
$2M_J$	A_{band}	5.89	3.77	2.37	1.31	1.02	1.84	5.89	3.77	2.37	1.31	1.02	1.84
	$Mag_{expected}$	19.69	16.64	14.07	12.34	11.62	11.18	24.05	21.89	19.90	16.04	13.77	13.70
	Mag_{pl}	11.28	10.29	9.52	9.05	9.34	8.35	17.63	17.27	17.33	14.29	12.57	11.84
$5M_J$	A_{band}	0.08	0.05	0.03	0.02	0.01	0.03	0.08	0.05	0.03	0.02	0.01	0.03
	$Mag_{expected}$	11.36	10.34	9.55	9.07	9.35	8.38	17.71	17.32	17.36	14.31	12.58	11.87
	Mag_{pl}	15.64	15.33	13.38	12.69	11.41	10.03	18.89	19.34	18.05	15.44	13.03	12.03
$1M_{inviscid}$	A_{band}	8.81	5.63	3.55	1.95	1.53	2.76	8.81	5.63	3.55	1.95	1.53	2.76
	$Mag_{expected}$	24.45	20.96	16.92	14.64	12.94	12.79	27.70	24.98	21.59	17.39	14.56	14.79

APPENDIX B: CONTRAST OF PLANETS EMBEDDED IN CQ TAU, HL TAU, TW HYA, AND HD 163296

The remaining contrast curves of planets as a function of the distance to the host star in the *J*, *H*, and *K* bands of all the studied systems are shown in Figs B1–B4: 0.94, 1.88, and $4.69M_J$ planets in the CQ Tau disc (Fig. B1); 0.44, 0.88, and $2.19M_J$ planets in HL Tau (Fig. B2); 0.47, 0.94, and $2.34M_J$ planets in TW Hya (Fig. B3); and 1.44, 2.88, and $7.19M_J$ planets in HD 163296 (Fig. B4).

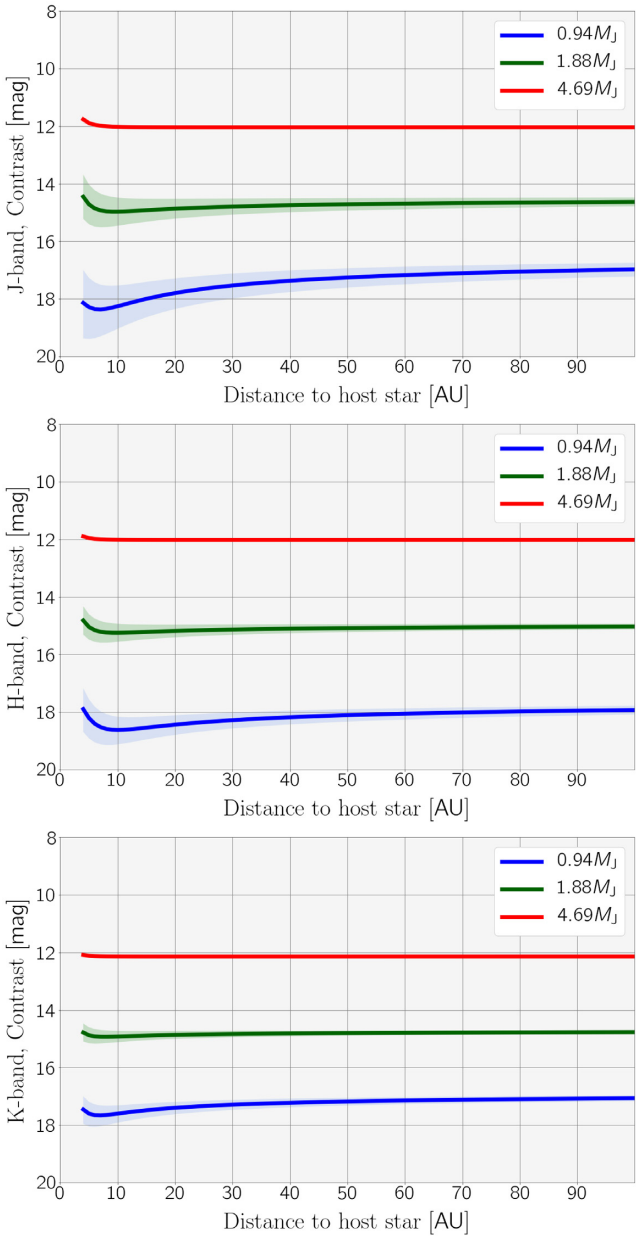

Figure B1. Contrast in the *J*, *H,* and *K* bands of planets embedded in the CQ Tau disc as a function of distance to the central star . Results are for planets with masses 0.94, 1.88, and 4.69M_J.

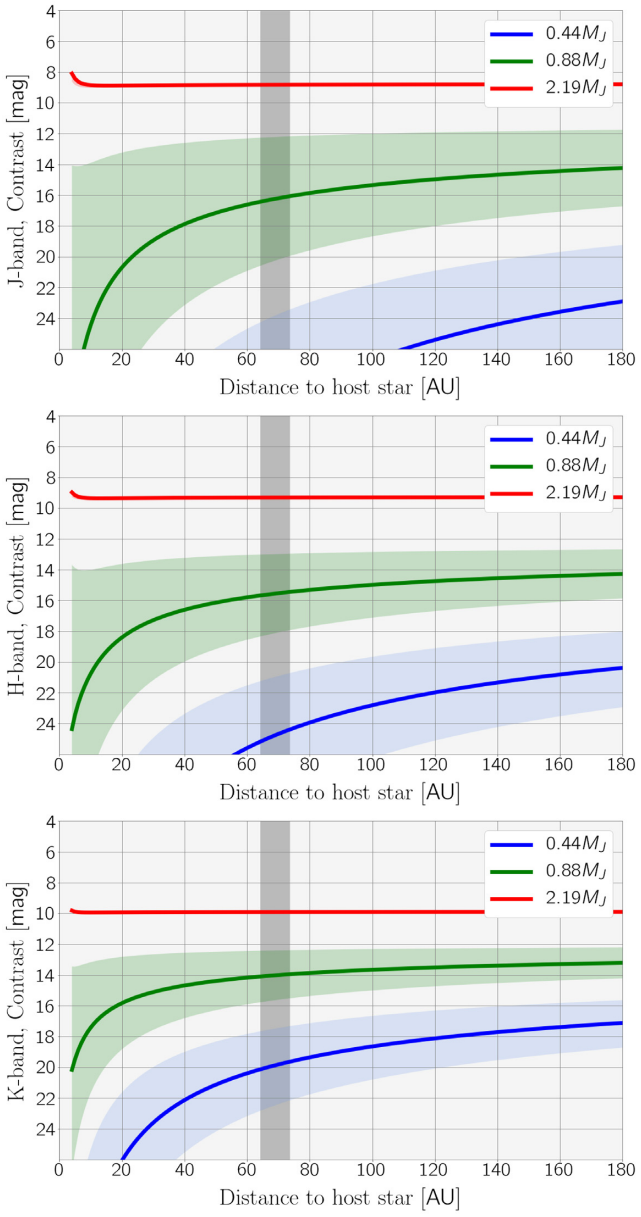

Figure B2. Application of our model to planets with masses 0.44, 0.88, and 2.19M_J embedded in the HL Tau disc. Contrast is shown for different distances to the host star in the *J*, *H,* and *K* bands.

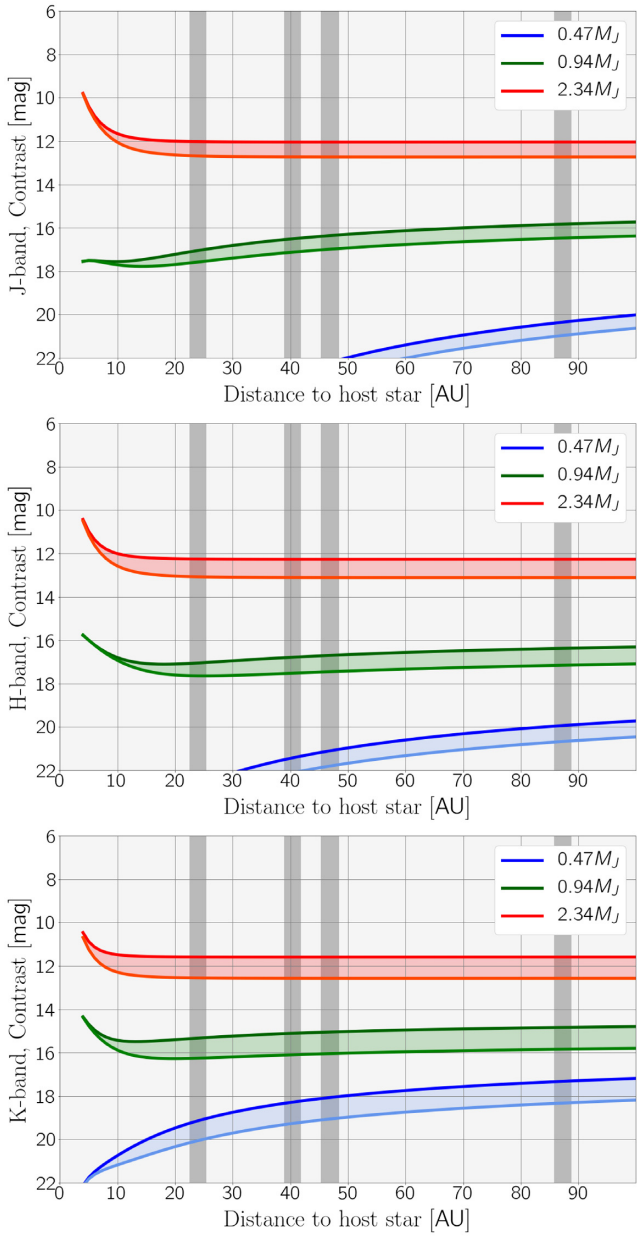

Figure B3. Application of our model to planets with masses 0.47, 0.94, and 2.34M_J embedded in the TW Hya disc. Contrast is shown for different distances to the host star in the *J*, *H,* and *K* bands.

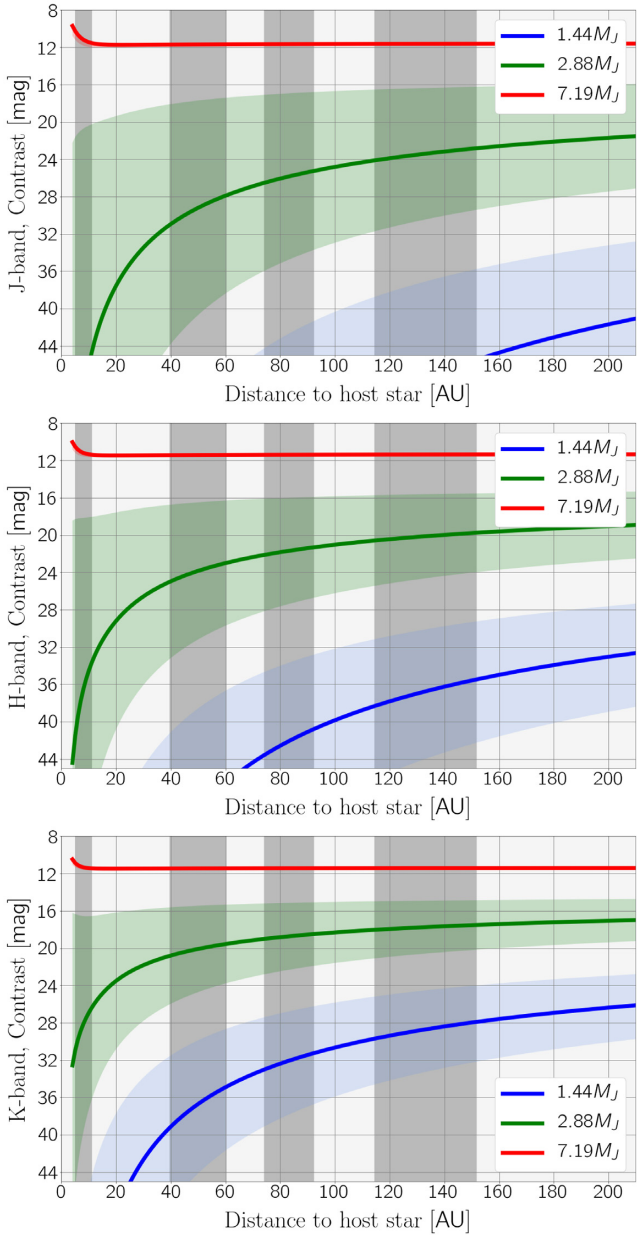

Figure B4. Application of our model to planets with masses 1.44, 2.88, and 7.19M_J embedded in the HD 163296 disc. Contrast is shown for different distances to the host star in the *J*, *H,* and *K* bands.

This paper has been typeset from a TEX/LATEX file prepared by the author.